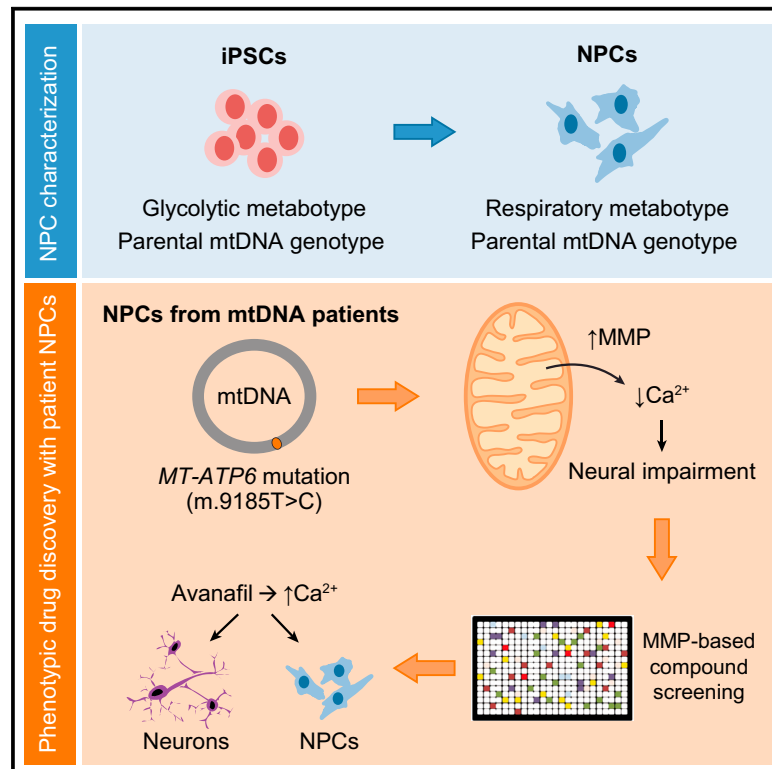# Human iPSC-Derived Neural Progenitors Are an Effective Drug Discovery Model for Neurological mtDNA Disorders

Graphical Abstract

Authors

Carmen Lorenz, Pierre Lesimple,
Raul Bukowiecki, ..., Erich E. Wanker,
Anne Lombès, Alessandro Prigione

Correspondence

anne.lombes@inserm.fr (A.L.),
alessandro.prigione@mdc-berlin.de (A.P.)

In Brief

Prigione and colleagues show that neural progenitors differentiated from patient-derived iPSCs are an effective modeling tool for neuronal disease associated with mtDNA mutations and can be used for drug screening.

Highlights

- iPSC-derived neural progenitors develop neuronal-like mitochondrial metabolism

- Derived NPCs retain parental mtDNA sequences and model mutant phenotypes

- Altered calcium homeostasis is a candidate pathological mechanism

- Drug screening based on mitochondrial phenotypes rescues calcium defects

CellPress

Cell Stem Cell

Article

CellPress

Human iPSC-Derived Neural Progenitors Are an Effective Drug Discovery Model for Neurological mtDNA Disorders

Carmen Lorenz,[1,2,12] Pierre Lesimple,[3,4,5,12] Raul Bukowiecki,[1] Annika Zink,[1,6] Gizem Inak,[1] Barbara Mlody,[1] Manvendra Singh,[1] Marcus Semtner,[1] Nancy Mah,[6] Karine Auré,[3,4,5] Megan Leong,[1] Oleksandr Zabiegalov,[1] Ekaterini-Maria Lyras,[6] Vanessa Pfiffer,[1] Beatrix Fauler,[7] Jenny Eichhorst,[9] Burkhard Wiesner,[9] Norbert Huebner,[1] Josef Priller,[2,6,8] Thorsten Mielke,[7] David Meierhofer,[7] Zsuzsanna Izsvák,[1] Jochen C. Meier,[1,10] Frédéric Bouillaud,[3,4,5] James Adjaye,[11] Markus Schuelke,[6] Erich E. Wanker,[1] Anne Lombès,[3,4,5,*] and Alessandro Prigione[1,13,*]

[1]Max Delbrueck Center for Molecular Medicine (MDC), 13125 Berlin, Germany
[2]Berlin Institute of Health (BIH), Berlin 10117, Germany
[3]INSERM U1016, Institut Cochin, Paris 75014, France
[4]CNRS UMR 8104, Paris 75014, France
[5]Université Paris Descartes, Paris 75006, France
[6]Charité − Universitätsmedizin, Berlin 10117, Germany
[7]Max Planck Institute for Molecular Genetics, Berlin 14195, Germany
[8]DZNE, Berlin 10117, Germany
[9]Leibniz Institut für Molekulare Pharmakologie (FMP), Berlin 13125, Germany
[10]Zoological Institute, Braunschweig 38106, Germany
[11]Institute for Stem Cell Research and Regenerative Medicine, Medical Faculty, Heinrich Heine University, Düsseldorf 40225, Germany
[12]Co-first author
[13]Lead Contact
*Correspondence: anne.lombes@inserm.fr (A.L.), alessandro.prigione@mdc-berlin.de (A.P.)
http://dx.doi.org/10.1016/j.stem.2016.12.013

SUMMARY

Mitochondrial DNA (mtDNA) mutations frequently cause neurological diseases. Modeling of these defects has been difficult because of the challenges associated with engineering mtDNA. We show here that neural progenitor cells (NPCs) derived from human induced pluripotent stem cells (iPSCs) retain the parental mtDNA profile and exhibit a metabolic switch toward oxidative phosphorylation. NPCs derived in this way from patients carrying a deleterious homoplasmic mutation in the mitochondrial gene MT-ATP6 (m.9185T>C) showed defective ATP production and abnormally high mitochondrial membrane potential (MMP), plus altered calcium homeostasis, which represents a potential cause of neural impairment. High-content screening of FDA-approved drugs using the MMP phenotype highlighted avanafil, which we found was able to partially rescue the calcium defect in patient NPCs and differentiated neurons. Overall, our results show that iPSC-derived NPCs provide an effective model for drug screening to target mtDNA disorders that affect the nervous system.

INTRODUCTION

Approximately 1 in 5,000 individuals (Gorman et al., 2015) suffers from deleterious mtDNA mutations that can cause metabolic disorders and typically lead to dysfunctions of the nervous system

(Carelli and Chan, 2014). Recent breakthroughs in the field of mitochondrial medicine might yield methods to prevent the transmission of pathogenic mtDNA mutations in the future (Mitalipov and Wolf, 2014; Reddy et al., 2015); but, currently no cures or effective interventional therapies are available for patients who have already inherited the mutations and are subject to such disorders (Pfeffer et al., 2013).

The development of new treatment options has been hampered by a lack of relevant models for mtDNA-related diseases, largely due to the challenges of engineering mtDNA. mtDNA mutations can be introduced into mouse germ cells (Inoue et al., 2000), or they can be induced to occur as a consequence of a proofreading-deficient DNA polymerase gamma (Kauppila et al., 2016). However, the generated mouse models cannot recapitulate the heteroplasmy or tissue specificity of mtDNA disorders. The most important cellular models of mtDNA diseases are based on cytoplasmic hybrids (cybrids), obtained by fusing immortalized human cell lines depleted of mtDNA with patient-derived enucleated cells. These models have permitted the identification of some of the cellular and molecular consequences that follow from mutations in mtDNA (King and Attardi, 1989). But cybrids cannot address the effects that result from the interplay between mitochondrial DNA and specific characteristics of an individual patient's nuclear DNA, which have been shown to influence the course of these diseases (Bénit et al., 2010; D'Aurelio et al., 2010). Additionally, the bioenergetics of cybrids depend on glycolysis, whereas the neuronal cells that are symptomatic rely on mitochondrial oxidative phosphorylation (OXPHOS) (Abramov et al., 2010; Carelli and Chan, 2014). These significant differences limit the extent to which cybrids can be used as models in searching for new types of therapies.
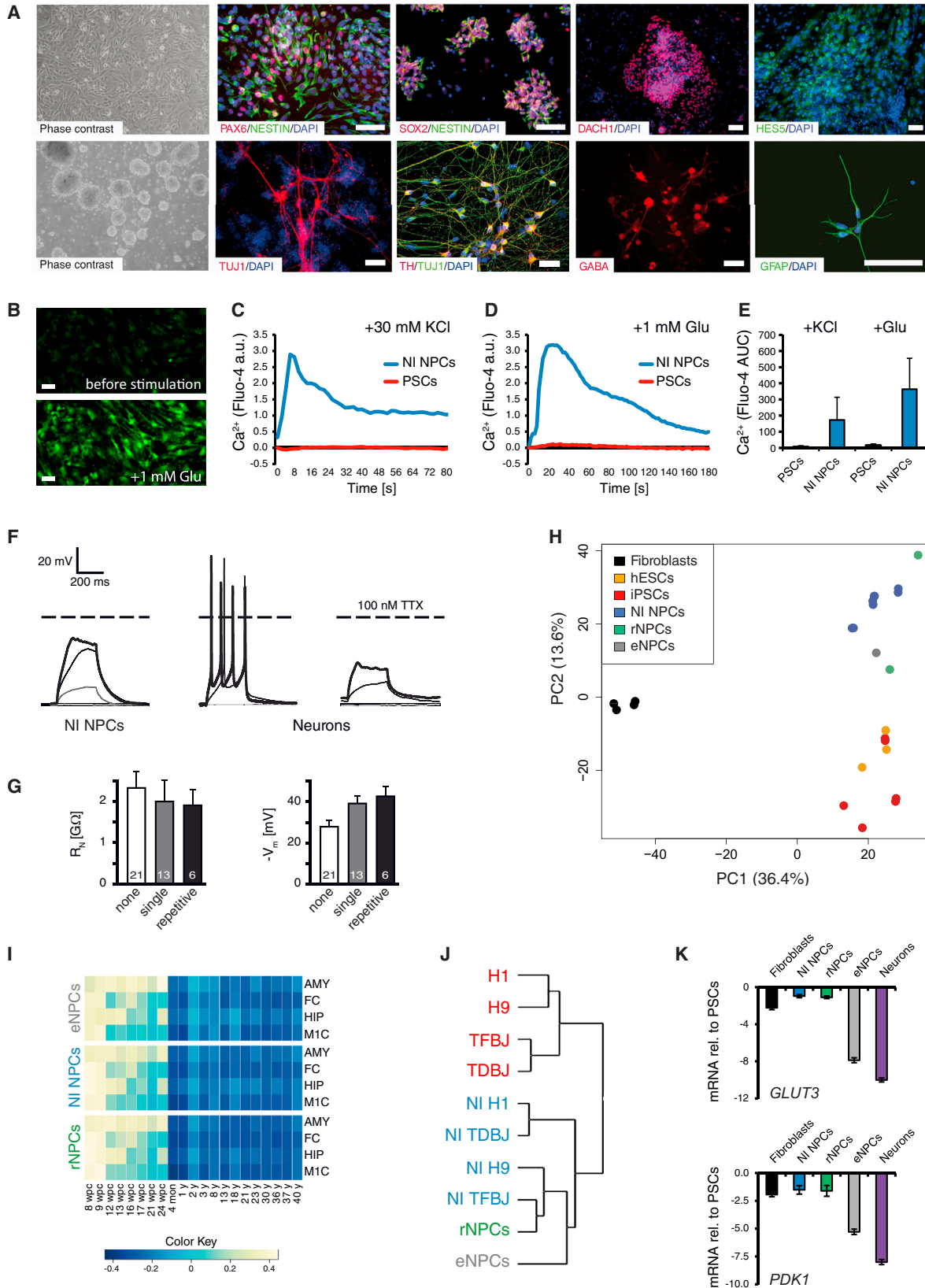
(legend on next page)

Here we suggest an innovative, more potent alternative in the form of neural progenitor cells (NPCs), which have the characteristics needed in a model to study neurological diseases caused by mtDNA mutations and set up drug discovery pipelines to treat them. NPCs can be rapidly obtained from induced pluripotent stem cells (iPSCs), either through an intermediate generation of rosettes (Koch et al., 2009) or the direct application of a cocktail of small molecules (Li et al., 2011; Reinhardt et al., 2013). We previously have shown that mitochondria undergo morphological and metabolic reconfigurations upon the generation of iPSCs (Prigione et al., 2010). Here we further demonstrate that, when iPSCs are put through the steps of neural induction to become NPCs, their mitochondria undergo maturation and a metabolic shift toward neuronal-like oxidative metabolism, while entirely retaining the mitochondrial genome of the parent cell from which they were originally derived.

To examine whether NPCs represent a valid cellular system for compound screening approaches for mtDNA diseases, we generated iPSC-derived NPCs from three patients carrying the mutation m.9185T>C in the *MT-ATP6* gene for ATP synthase (complex V) in a homoplasmic state (i.e., affecting all mtDNA molecules). This mutation is a recurrent cause of neurological diseases such as Leigh syndrome (Moslemi et al., 2005), neuropathy, ataxia, retinitis pigmentosa (NARP) (Childs et al., 2007), and episodic paralysis with spinal neuropathy (Auré et al., 2013). Patient-derived NPCs exhibited functional alterations, including decreases in ATP production, abnormally high mitochondrial membrane potential (MMP), and altered calcium homeostasis. We developed a high-content screening (HCS) strategy based on the patient MMP phenotype, and we used it to screen a library of FDA-approved compounds. The phosphodiesterase type 5 (PDE5) inhibitor avanafil, a compound that reduced the mitochondrial hyperpolarization, also partially rescued the calcium defect in both patient NPCs and differentiated neurons. These findings suggest that iPSC-derived NPCs represent an effective model system to analyze mechanisms underlying mtDNA-related neurological disorders and to carry out personalized phenotypic drug discovery for diseases that have been untreatable until now.

RESULTS

Functional Assessments of Neurally Induced Neural Progenitor Cells

A small molecule-based protocol (Li et al., 2011) was used to facilitate neural induction of human pluripotent stem cells (PSCs), bypassing rosette derivation (Koch et al., 2009), which is time consuming and operator-dependent (Figure S1A). Neurally induced neural progenitor cells (NI NPCs) were obtained from the human embryonic stem cell (hESC) lines H1 and H9, control iPSCs derived via transfection (TF) of episomal vectors, and control iPSC lines previously generated via retroviral transduction (TD) (Prigione et al., 2010, 2011a, 2011b) (Figures S1B–S1H). NI NPCs grew as a uniform monolayer, expressed NPC marker proteins, retained their multipotent identity for over 30 passages, and were capable of generating neuronal and glial subtypes, including GABAergic neurons, dopaminergic neurons, and astrocytes (Figure 1A).

NI NPCs functionally responded to calcium mobilization, following voltage-dependent (high potassium chloride) and receptor-dependent (glutamate) stimuli (Figures 1B–1E; Movie S1). These stimuli led to the influx of calcium into the cells and subsequent calcium-induced calcium release from intracellular stores. In contrast, no response was provoked in undifferentiated iPSCs or hESCs (Figures 1B–1E). This suggested that NI NPCs might be suitable models for an investigation of calcium-regulated mechanisms. Whole-cell patch-clamp recordings in the current clamp mode were performed on NI NPCs and neurons at various time points of differentiation. In maturing neuronal-like cells, single and repetitive action potentials appeared after 8–12 weeks of differentiation (Figures S1I and S1J). Depolarizing currents failed to induce a firing of action potentials in NI NPCs (Figure 1F). Membrane potentials and resistance, on the other

Figure 1. Generation of NI NPCs

(A) Upper panel: spiked morphology of NI NPCs and expression of NPC markers PAX6, SOX2, NESTIN, DACH1, and HES5. Lower panel: neurospheres from NI NPCs and differentiated neurons (TUJ1 positive), including dopaminergic (TH positive) and GABAergic neurons (GABA positive), and astrocytes (GFAP positive) are shown. Scale bar, 100 μm.

(B) Representative images of NI NPCs (line NI H1) show cytosolic calcium before stimulation and at maximal peak Fluo-4 fluorescence after 1 mM glutamate (Glu) stimulus. Scale bar, 50 μm.

(C and D) Cytosolic calcium monitored in PSCs and NI NPCs following voltage-mediated (C, 30 mM KCl) and receptor-mediated (D, 1 mM glutamate, Glu) stimuli. Time point zero corresponds to stimuli administration. The profiles represent the average of PSCs (H1, H9, and TFBJ) and corresponding NI NPCs (three biological replicates each).

(E) Calcium responses were quantified by determining the area under the curve (AUC) of Fluo-4 fluorescence profiles.

(F) Patch-clamp recordings in NI NPCs and neurons and the effect of 100 nM tetrodotoxin (TTX) (shown here for line NI H1) are shown.

(G) Membrane resistance (R_N) and membrane potential ($-V_m$) during the course of differentiation (from NI H1 and NI TFBJ). Populations were separated into "none" (n = 21 of three biological replicates), "single" (n = 13), and "repetitive" (n = 6) action potential firing cells.

(H) Principal-component analysis (PCA) showing the transcriptomic clustering of fibroblasts (BJ, HFF1), hESCs (H1 and H9), iPSCs (TFBJ, TDBJ5, and TDHFF1), NI NPCs (NI H1, NI H9, NI TDBJ5, and NI TFBJ), rNPCs, and eNPCs. Probe sets were filtered for at least one present call and with an interquartile range (IQR) > 25th percentile.

(I) Mapping of the transcriptomic data of NI NPCs, eNPCs, and rNPCs onto the Allen Human Brain Atlas. Color key displays the range of pairwise ranked correlation between analyzed sample matrix. Columns designate different time periods in the pre- and postnatal phases (wpc, week post-conception) and rows specify brain areas (AMY, amygdala; FC, frontal cortex; HIP, hippocampus; M1C, primary motor cortex).

(J) Clustering was performed using genes known to regulate energy metabolism.

(K) qPCR expression analysis of two glycolytic regulators in fibroblasts (BJ and HFF1), NI NPCs (NI H1, NI H9, NI TDBJ5, and NI TFBJ), rNPCs, eNPCs, and neurons (from NI H1 and NI TFBJ). Values are presented as Log2 of the ratio between the expression values of *GLUT3* or *PDK1* over *ACTB* in relation to the undifferentiated PSC line H1.

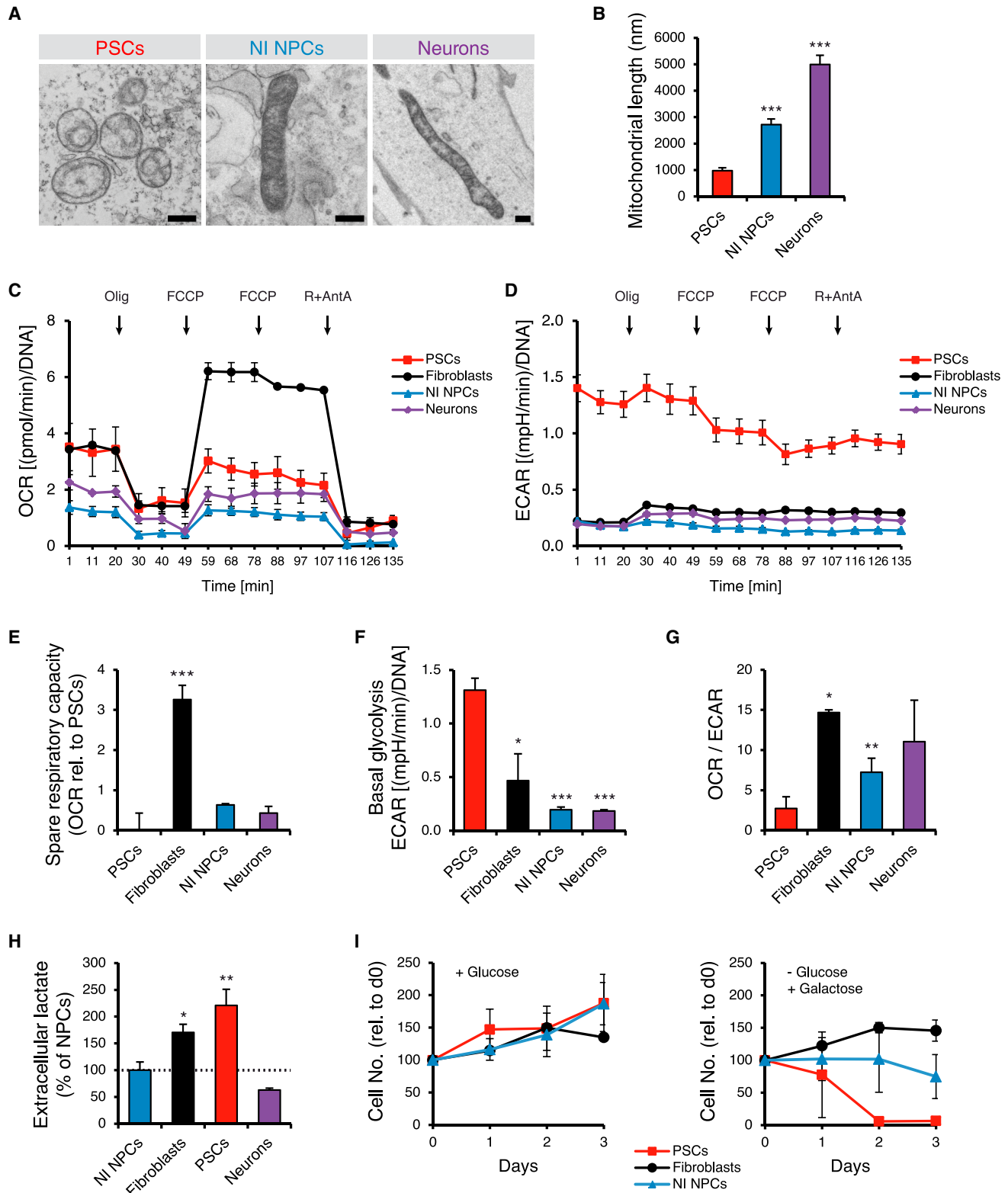See also Figures S1 and S2, Table S1, and Movie S1.

Figure 2. Mitochondrial and Metabolic Reconfiguration upon Neural Induction

(A) Transmission electron microscopy (TEM) images show the morphology of mitochondria within PSCs, NI NPCs, and differentiated neurons (shown are H1, NI H1, and neurons from NI H1). Scale bar, 500 nm.

(legend continued on next page)

hand, did not change significantly upon differentiation (Figure 1G). This indicated that, although NI NPCs do not fire action potentials upon depolarization, their passive electrical properties are close to those of differentiated neuronal-like cells.

Principal-component analysis (PCA) demonstrated that the transcriptome of NI NPCs was similar to that of NPCs generated using the traditional rosette-based approach (rNPCs) or obtained from ex vivo adult human brain (eNPCs) (Figure 1H; Figure S2A). This also was confirmed by comparing our data with previously published NPC transcriptomes (Brennand et al., 2011; Hargus et al., 2014; Li et al., 2011; Reinhardt et al., 2013; Stein et al., 2014) (Figure S2B). A pathway analysis of the uniquely expressed genes in NI NPCs, rNPCs, and eNPCs revealed that eNPCs exhibited a higher commitment toward neuronal development compared to the other PSC-derived NPCs (Figures S2C and S2D; Table S1). Nonetheless, NI NPCs, rNPCs, and eNPCs displayed a highly comparable pattern once mapped onto the human brain atlas (Figure 1I). Hence, PSC-derived NPCs may sufficiently represent NPCs that reside in the adult human brain.

NI NPCs Exhibit Mitochondrial Maturation and Neuronal-like Energy Metabolism

The generation of iPSCs is accompanied by an extensive restructuring of mitochondria and energy metabolism (Folmes et al., 2011; Prigione et al., 2010). A hierarchical clustering of genes involved in energy metabolism (Prigione et al., 2011b) identified differences in the metabolic regulation of PSCs and NPCs (including NI NPCs, rNPCs, and eNPCs) (Figure 1J). Clustering the samples according to OXPHOS genes produced the same pattern (data not shown). This suggests that NPCs may regulate cellular bioenergetics fundamentally differently from PSCs, irrespective of the mode by which they were derived. The qPCR data confirmed that glycolytic regulators, such as *GLUT3* and *PDK1*, were downregulated in NPCs and neurons in comparison to PSCs, indicating that neural induction is accompanied by a reduction of glycolytic metabolism (Figure 1K).

Transmission electron microscopy showed that the mitochondria of NI NPCs display a fused ultrastructural morphology with well-developed cristae, resembling those of neurons but differing from the ultrastructure of PSC mitochondria (Figure 2A). In accordance, there was a significant increase in mitochondrial length during neural induction (Figure 2B).

We used Seahorse technology, which concomitantly measures respiration (oxygen consumption rate [OCR]) and glycolysis

(extracellular acidification rate [ECAR]), to compare the bioenergetic profiles of NI NPCs and neurons to those of PSCs and fibroblasts (Figures 2C and 2D). The rates of basal and maximal respiration and proton leak were similar in all cell types except fibroblasts, whose maximal respiration was higher (Figures S2E–S2G). Fibroblasts also had a much higher spare respiratory capacity than NI NPCs and neurons, in which the levels were only slightly higher than those of PSCs (Figure 2E). Conversely, NI NPCs and neurons experienced a sharp reduction in basal glycolysis compared to PSCs. This reduction was highly significant and more pronounced than that seen in fibroblasts (Figure 2F). This seems to indicate that neural induction is associated with a strong decrease of glycolytic metabolism. Accordingly, the OCR/ECAR ratio increased to a similar degree in fibroblasts, NI NPCs, and neurons compared to PSCs, suggesting a predominance of OXPHOS over glycolysis in these cell types (Figure 2G). This finding was supported by the lower amounts of extracellular lactate found in NI NPCs and neurons than in PSCs (Figure 2H). The fact that NI NPCs could be maintained in glucose-free galactose medium, which requires using OXPHOS (Figure 2I), is further evidence of a lower dependence on glycolysis.

These data suggest that neural induction triggers mitochondrial maturation, leading to an oxidative metabolic state in NI NPCs, which resembles that of neurons.

NI NPCs Retain Their Parental mtDNA Sequence Profile

To make useful models of mitochondrial diseases from NI NPCs, we needed to exclude the possibility that mtDNA had undergone changes during stages of induction, as can happen in the generation of iPSCs (Ma et al., 2015; Prigione et al., 2011b). We performed Sanger sequencing of the entire mtDNA, using long-range PCR with nested primers to exclude nuclear mtDNA pseudogenes. We analyzed BJ control fibroblasts, BJ-derived TD-iPSCs, BJ-derived TF-iPSCs, hESCs, and the NI NPCs generated from the PSCs.

We found that the specific mtDNA variants from each individual were fully retained upon iPSC derivation, regardless of the reprogramming method that was used. This was also true upon neural induction (Figure 3A; Table S2), irrespective of the type of variant and its location within the mtDNA sequence (Figure 3B). Remarkably, even the spectrum of D310 tract heteroplasmy in the hypervariable region of the D-loop (mtDNA nucleotides 57–372) was preserved through these stages (Figure 3C) (its high heterogeneity makes it a common tool for forensic fingerprinting).

(B) Mitochondrial length was quantified in PSCs (H1, H9, TDHFF1, TDBJ4, TDBJ5, and TFBJ), NI NPCs (NI H1, NI H9, NI TDBJ5, and NI TFBJ), and neurons (from NI TFBJ) (at least 60 mitochondria per cell line, out of at least 20 TEM images).

(C) Oxygen consumption rate (OCR) profile, using the Seahorse XF24 Analyzer for PSCs (H1, H9, and TFBJ), fibroblasts (BJ and HFF1), NI NPCs (NI H1, NI H9, and NI TFBJ), and neurons (from NI H1 and NI TFBJ) (at least two biological replicates per line, each with at least three technical replicates), is shown. Olig, 1 μM oligomycin; FCCP, 1 μM FCCP; R+AntA, 1 μM rotenone + 1 μM antimycin A.

(D) Extracellular acidification rate (ECAR) profile, reflecting glycolytic activity, was measured in parallel to OCR.

(E–G) Spare respiratory capacity (E, shown in relation to PSCs), basal glycolysis (F), and OCR/ECAR ratio (G) were calculated from the Seahorse profiling. Statistics refer to PSCs.

(H) Extracellular lactate content in PSCs (H1, H9, and TFBJ), fibroblasts (BJ and HFF1), NI NPCs (NI H1, NI H9, and NI TFBJ), and neurons (from NI H1 and NI TFBJ) (at least two biological replicates per line, each with at least seven technical replicates) is shown.

(I) Cellular proliferation in 25 mM glucose (+ glucose) or in 10 mM galactose (− glucose + galactose) for PSCs (H1 and TFBJ), NI NPCs (NI H1, NI H9, and NI TFC1), and fibroblasts (BJ and HFF1) (at least two biological replicates per line, each with at least three technical replicates; error bars represent SD). In all panels, unless otherwise indicated, error bars represent SEM and p values were determined by unpaired two-tailed Student's t tests (*p ≤ 0.05, **p ≤ 0.01, and ***p ≤ 0.001). See also Figure S2.

A

Sample	Total variants	Homoplasmic	Heteroplasmic	D-loop	mRNA	tRNA	rRNA
H1	17	14	3	6	6	0	5
NI H1	17	14	3	6	6	0	5
H9	37	36	1	10	20	2	5
NI H9	37	36	1	10	20	2	5
BJ	34	32	2	9	19	1	5
TDBJ4	34	32	2	9	19	1	5
TDBJ5	34	32	2	9	19	1	5
TFBJ.2	34	32	2	9	19	1	5
TFBJ	34	32	2	9	19	1	5
NI TDBJ5	34	32	2	9	19	1	5
NI TFBJ	34	32	2	9	19	1	5

B

BJ - TDBJ5 - NI TDBJ5

C

D

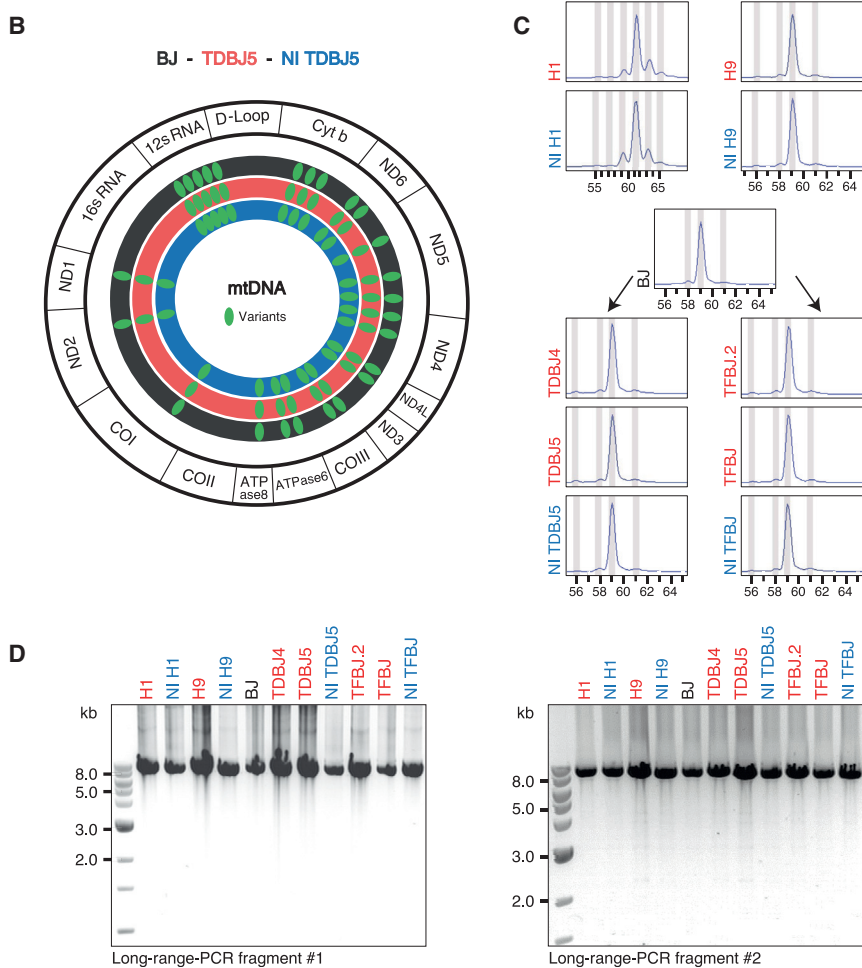Long-range-PCR fragment #1

Long-range-PCR fragment #2

Figure 3. Preservation of mtDNA during Reprogramming and Neural Induction

(A) Number of variants identified with whole-mtDNA sequencing in fibroblasts (black), PSCs (red), and NI NPCs (blue) is shown.

(B) Location of mtDNA variants (green ovals) in BJ fibroblasts (black circle), BJ-derived iPSC line TDBJ5 (red circle), and TDBJ5-derived NI TDBJ5 (blue circle) is shown.

(C) Preservation of the D310 tract heteroplasmy is shown within the hypervariable region of the D-loop (mtDNA nucleotides 57–372) in two hESCs and their related NI NPCs, in BJ fibroblasts, BJ-derived retroviral-based (TDBJ4 and TDBJ5) and plasmid-based (TFBJ and TFBJ.2) iPSC lines, and their respective NI NPCs.

(D) Two different long-range PCR sets were used to exclude the presence of mtDNA deletions within PSCs and related NI NPCs.

See also Table S2.

bolism (Figures 2A–2I), and retain the parental mtDNA profile (Figures 3A–3D). To replicate these findings in a real-case scenario, we derived NI NPCs from three patients from a family that harbors the homoplasmic mutation m.9185T>C in the *MT-ATP6* gene (Auré et al., 2013) (Figures S3A–S3F). The cells, to which we assigned the common designation NPC_ATP6, comprised NI A1 (derived from the iPSC line TFA1), NI A2 (from the iPSC line TDA2.3), and NI A3 (from the iPSC line TDA3.1), and expressed the correct NPC protein markers (Figure 4A).

We used whole-mtDNA sequencing and restriction fragment length polymorphism (RFLP) analysis to demonstrate that NPC_ATP6 retained the mtDNA of the original fibroblasts. The cells exhibited homoplasmic levels of the m.9185T>C mutation without any additional mtDNA mutations (Figures 4B and 4C; Figures S4A–S4C). NPC_ATP6 also maintained intact versions of the parental D310 hypervariable regions of the D-loop and did not undergo any mtDNA deletions, as demonstrated using two distinct long-range PCR sets (Figures S4D–S4F). This means that any cellular phenotypes in NPC_ATP6 that are driven by the mitochondrial genome can be solely attributed to the patient-specific *MT-ATP6* mutation.

Finally, in contrast to a recent report on hESCs (Van Haute et al., 2013), we did not observe the occurrence of large mtDNA deletions in PSCs (including hESCs, TD-iPSCs, and TF-iPSCs) or NI NPCs. (Figure 3D). These results demonstrate that NI NPCs can maintain the mtDNA profile of the primary cells from which they are derived.

Generation of Patient NI NPCs Carrying a Homoplasmic *MT-ATP6* Mutation

NI NPCs may represent a bona fide model system for mtDNA-related neurological diseases because they share features with brain-derived neural cells (Figure 1I), rely on mitochondrial meta-

Bioenergetic Consequences of the Homoplasmic *MT-ATP6* Mutation

Direct measurements of ATP production in permeabilized NPC_ATP6 cells revealed a significant defect (Figure 4D) similar to that found in the primary fibroblasts from which they were obtained (Fib_ATP6) and in three independent cybrid clones

CellPress

derived from A1 fibroblasts (Cyb_ATP6) (Figure 4D). In spite of this, we found unaffected steady-state levels of ATP in intact NPC_ATP6, whether grown under standard conditions or after 4 hr in starvation medium, as well as in intact Fib_ATP6 and Cyb_ATP6 (Figure 4E). Accordingly, the reduced production of ATP in NPC_ATP6 did not affect the cells' metabolic profile under basal or starvation states, as assessed with Seahorse technology (Figures S5A–S5D) or their extracellular lactate content (Figure S5E). This suggests that cells carrying the m.9185T>C mutation had efficiently adapted their energy expenditure to the lower levels of ATP. This behavior also is encountered in physiological conditions of energy shortage (Staples and Buck, 2009), and it is also in agreement with clinical observations (Campbell and Marcinek, 2016). One of these cellular adjustments probably involves the partial depolarization of the plasma membrane (Auré et al., 2013), as we observed in NPC_ATP6 using electrophysiology analysis (Figure 4F).

The proliferation rates of NPC_ATP6, Fib_ATP6, and Cyb_ATP6 were likewise unaffected in glucose medium or during the shift of cellular metabolism toward OXPHOS in galactose medium (Figure 4G). NPC_ATP6 appeared to have normal mtDNA copy number (Figure S5F) and mitochondrial ultrastructure and distribution (Figures S5G and S5H). Measurements of the kinetics of MitoSox signal revealed no change in the production of superoxide ions in NPC_ATP6 and Cyb_ATP6, in contrast to significant increases that have been observed previously in Fib_ATP6 (Figure 4H) (Auré et al., 2013). These findings suggest that distinct cell types find different ways of responding to the same bioenergetic challenge. So, in seeking the mechanisms responsible for the neural impairment associated with MT-ATP6 mtDNA mutations, neural-like cells should be used (Abramov et al., 2010).

Mitochondrial Hyperpolarization in Neural Cells Carrying the MT-ATP6 Mutation

We next used a permeabilization-based method to measure the MMP of NPC_ATP6, Fib_ATP6, and Cyb_ATP6. We observed an increase of MMP, as expected, in the presence of ADP, which is the substrate of ATP synthase that induces state 3 respiration (Figures S6A–S6C). Treating all permeabilized cells with oligomycin, an inhibitor of ATP synthase that induces state 4 respiration, revealed normal MMP (Figures S6A–S6C). Importantly, the drop in MMP was significantly decreased in individual NPC_ATP6 (Figure 5A). The significance of the change was lower in mutant cybrids and did not reach significance in patient fibroblasts (Figure 5A). This suggests that NPCs might not regulate MMP as efficiently as either fibroblasts or cybrids.

Next we carried out an imaging-based assessment of MMP in live, intact cells. This revealed a significant, abnormal increase in MMP in NPC_ATP6 cells, but not in Fib_ATP6 or Cyb_ATP6 cells (Figure 5B). To control for technical bias, we demonstrated that oligomycin induced similar increases in the MMP signal in the three cell types (Figure S6D). Notably, neurons derived from patient NPCs (Neur_ATP6) also exhibited mitochondrial hyperpolarization (Figure 5C). We could exclude differentiation defects as the cause, since populations of Neur_ATP6 and control neurons (Neur_Ctrl) had a similar number of TUJ1-positive cells (Figure 5D; Figure S6E). Furthermore, the mitochondria of Neur_ATP6 had normal morphology and lengths compared to

Neur_Ctrl (Figures 5E and 5F). This means that the phenotypes observed in differentiated neurons replicated those observed in NI NPCs, including the abnormal MMP increase.

MT-ATP6 mutation may thus specifically disrupt the ability of neural cells (including both neural progenitor cells and postmitotic neurons) to control MMP under basal conditions, an effect that is not seen in cybrids or fibroblasts.

Altered Mitochondrial Calcium Homeostasis in Patient NPCs

To gain further insights into the pathophysiology of the MT-ATP6 mutation, we interrogated the global transcriptome of control and patient NPCs (Table S1). We found a variable modulation of the expression of genes encoding for mitochondrial complexes, which supported our bioenergetic findings and excluded a uniform functional transcriptional compensatory response in NPC_ATP6 (Figure S6F). On the other hand, genes involved in mitochondrial calcium homeostasis were consistently downregulated in NPC_ATP6 (Figure S6G). A cluster analysis of these genes permitted us to observe patterns that clearly distinguished patient-derived NI NPCs from control NI NPCs. In particular, NPC_ATP6 showed significant downregulation of LETM1 in the inner mitochondrial membrane, VDAC3 in the outer mitochondrial membrane, and ATP5O, which encodes for oligomycin sensitivity-conferring protein (OSCP) whose decreased expression is associated with enhanced sensitivity of the permeability transition pore (PTP) to calcium (Giorgio et al., 2013) (Figure 6B). These disease-specific patterns were not found in PSCs or fibroblasts, which makes sense because those cells do not develop symptoms in the disease (Figure 6A).

A global proteomics analysis confirmed that calcium homeostasis was likely being altered in NPC_ATP6. A pairwise analysis revealed a downregulation of components of the calcium-signaling pathway in all three patient NPC lines compared to control lines (Figure 6C). Additional pathways that were downregulated in NPC_ATP6 related to the mitochondrial membrane and electron carrier activity (Figure S6H), while the apoptosis and p53/hypoxia pathways were upregulated compared to controls (Figure S6I).

Given the coherent picture of calcium dyshomeostasis from the -omics analyses, we set up calcium-imaging experiments to pursue its functional relevance. Stimulating NPC_ATP6 cells with glutamate led to decreased calcium-induced calcium release from intracellular stores (Figure 6D; Movie S2). To avoid effects dependent on the plasma membrane, which was partially depolarized in the patient cells (Figure 4F), we analyzed calcium homeostasis in permeabilized NI NPCs exposed to increasing doses of external calcium. NPC_ATP6 displayed a significant reduction in the acute increase of Fluo-4-labeled cytosolic calcium, which occurred after the third calcium addition (Figure 6E). This was also the case following treatment with a combination of FCCP and antimycin A, which depolarizes the MMP leading to the release of mitochondrial calcium into the cytosol (Figure 6F). In contrast, treatment with thapsigargin, which blocks calcium uptake resulting into calcium release from the endoplasmic reticulum, induced a similar cytosolic calcium increase in both patient and control NPCs (Figure 6G).
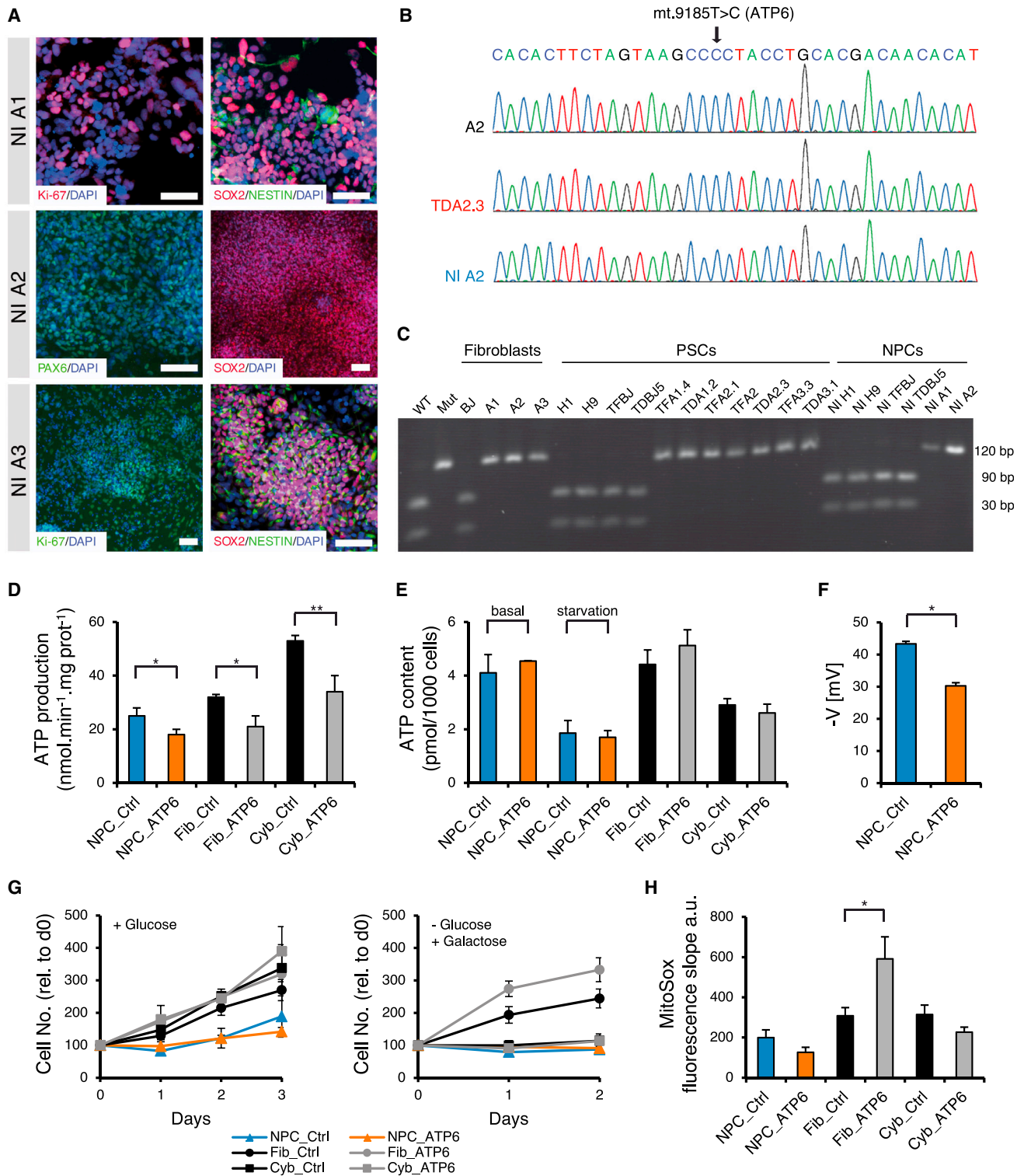
Figure 4. Generation of NPC_ATP6 Harboring the Mutation m.9185T>C

(A) NPC markers, SOX2, NESTIN, and PAX6, and proliferation marker Ki-67 in NPC_ATP6 are shown. Scale bar, 100 μm.

(B) Whole-mtDNA Sanger sequencing is shown for the area around the mutation m.9185T>C for patient A2 in fibroblasts, iPSCs, and NPCs.

(C) RFLP analysis confirms homoplasmic m.9185T>C mutation as a single 120-bp fragment (in control cells the restriction enzyme generates a 90-bp and a 30-bp fragment). WT, wild-type plasmid; Mut, mutant plasmid.
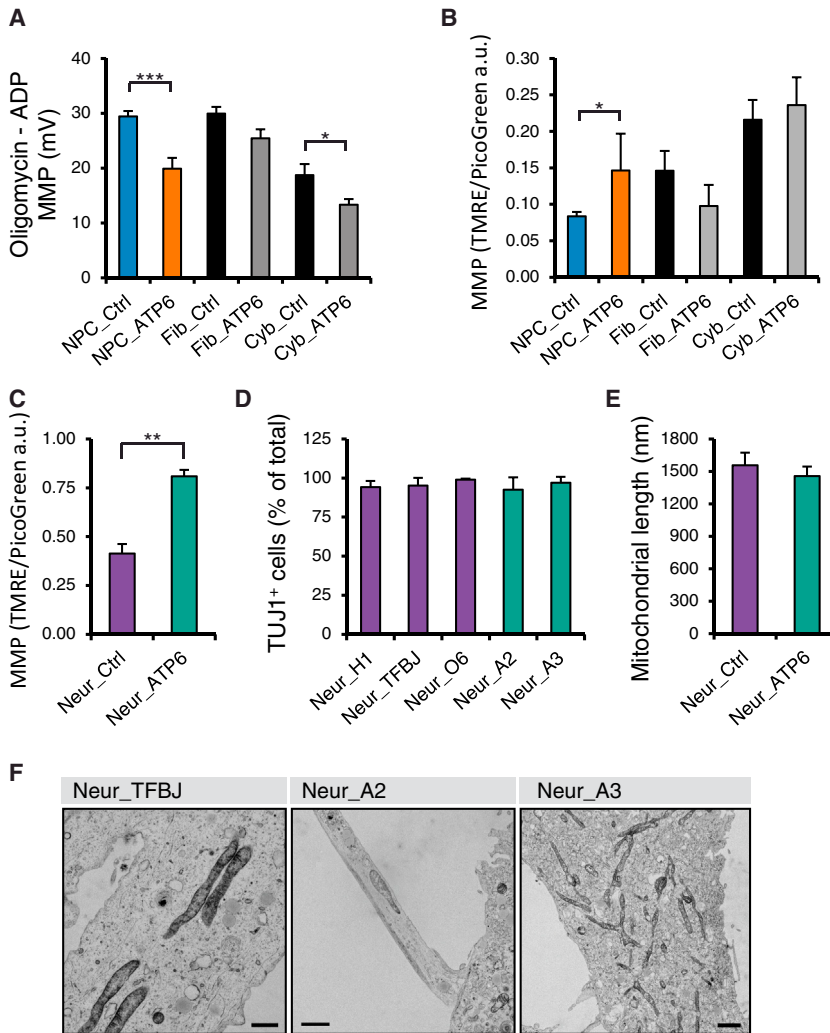
(legend continued on next page)

Figure 5. Mitochondrial Hyperpolarization in Neural Cells Carrying the *MT-ATP6* Mutation

(A) MMP quantification in permeabilized cells presented as the difference between state 4 respiration (induced by 1 μM oligomycin) and state 3 respiration (induced by 1 mM ADP) (see Figures S6A–S6C). At least three biological replicates per line were used: NPC_Ctrl (NI H1, NI H9, NI TFBJ, and NI TFC1), NPC_ATP6 (NI A1, NI A2, and NI A3), Fib_Ctrl (F20, F30, and EF10), Fib_ATP6 (A1, A2, and A3), Cyb_Ctrl (TFSR and 143B+), and Cyb_ATP6 (F06, F07, and F08) (see Figure S5L).

(B) Imaging-based assessment of MMP in intact cells in NPC_Ctrl (NI H1, NI H9, NI TFBJ, NI TDBJ5, NI O3, NI O6, NI TFC2, and NI TDHFF1), NPC_ATP6 (NI A1, NI A2, and NI A3), Fib_Ctrl (BJ, HFF1, NFH2, Con1, and LR), Fib_ATP6 (A1, A2, and A3), Cyb_Ctrl (TFSR and 143B+), and Cyb_ATP6 (F06, F07, and F08) (at least three biological replicates each, see Figure S5M). MMP was calculated by subtracting from the signal of untreated samples the signal obtained after treatment for 30 min with FCCP + antimycin A (both 1 μM).

(C) Imaging-based quantification of MMP in intact differentiated Neur_Ctrl (from NI H1, NI TFBJ, and NI O6) and Neur_ATP6 (from NI A2 and NI A3) is shown (two biological replicates each, see Figure S6F).

(D) High-content screening (HCS)-based quantification of TUJ1-positive cells in Neur_Ctrl (from NI H1, NI TFBJ, and NI O6) and Neur_ATP6 (from NI A2 and NI A3) is shown (n = 3 for each line).

(E) Mitochondrial length was measured in Neur_Ctrl (from NI TFBJ) and Neur_ATP6 (from NI A3) (at least 60 mitochondria each, out of at least 20 TEM pictures).

(F) Ultrastructure images of differentiated Neur_Ctrl (from NI TFBJ) and from Neur_ATP6 (from NI A2 and NI A3). Scale bar, 2 μm. In all panels, unless otherwise indicated, error bars represent SEM and p values were determined by unpaired two-tailed Student's t tests (*p ≤ 0.05, **p ≤ 0.01, and ***p ≤ 0.001). See also Figures S5 and S6.

Defects in the handling of calcium impair cellular functions, particularly in neuronal cells (Neher and Sakaba, 2008), which may help explain why symptoms arise specifically in the neurons of patients with ubiquitous *MT-ATP6* homoplasmic mutations. Moreover, the findings pointed to a specific alteration in mitochondrial calcium homeostasis, which is strongly influenced by the state of mitochondrial polarization (Rizzuto et al., 2012). This fits with our finding that Cyb_ATP6 achieves better MMP regulation (Figures 5A and 5B) and exhibits normal calcium responses (Figures 6H and 6I).

(D) ATP production is shown in permeabilized NPC_Ctrl (NI H1, NI H9, NI TDBJ5, NI TFBJ, NI TFC1, and NI TFLR), NPC_ATP6 (NI A1, NI A2, and NI A3), Fib_Ctrl (F20, F30, and EF10), Fib_ATP6 (A1, A2, and A3), Cyb_Ctrl (TFSR and 143B+), and Cyb_ATP6 (F06, F07, and F08) (at least three biological replicates each, see Figure S5I).

(E) ATP content is shown in intact cells in NPC_Ctrl (NI H1, NI H9, and NI TFBJ) and NPC_ATP6 (NI A1, NI A2, and NI A3) under basal condition and after 4-hr starvation, in Fib_Ctrl (BJ, HFF1, CON1, LR, and NFH2), in Fib_ATP6 (A1, A2, and A3), in Cyb_Ctrl (TFSR and 143B+), and in Cyb_ATP6 (F06, F07, and F08) (at least three biological replicates each, see Figures S5J and S5K).

(F) Resting plasma membrane potential in NPC_Ctrl (NI H1) and NPC_ATP6 (NI A2 and NI A3), each with at least four biological replicates, is shown.

(G) Proliferation curves of NPC_Ctrl (NI H1, NI TFBJ, NI TFC1, and NI LR), NPC_ATP6 (NI A1, NI A2, and NI A3), Fib_Ctrl (BJ, HFF1, CON1, LR, and NFH2), Fib_ATP6 (A1, A2, and A3), Cyb_Ctrl (TFSR and 143B+), and Cyb_ATP6 (F06, F07, and F08). Cells were kept in either standard medium containing 25 mM glucose (+ glucose) or in medium deprived of glucose containing 10 mM galactose (− glucose, + galactose) (at least two biological replicates each). Error bars represent SD.

(H) MitoSox fluorescence slope in NPC_Ctrl (NI H1, NI H9, and NI TFC1), NPC_ATP6 (NI A1, NI A2, and NI A3), Fib_Ctrl (EF1, EF10, EF9, EG1, EM2, FHN409, FHN505, and KB2), Fib_ATP6 (A1, A2, and A3), Cyb_Ctrl (TFSR, 143B+, EF9R, and VFR1), and Cyb_ATP6 (F06, F07, and F08) (at least three biological replicates each). In all panels, unless otherwise indicated, error bars represent SEM and p values were determined by unpaired two-tailed Student's t tests (*p ≤ 0.05, **p ≤ 0.01, and ***p ≤ 0.001). See also Figures S3–S5.

(legend on next page)

CellPress
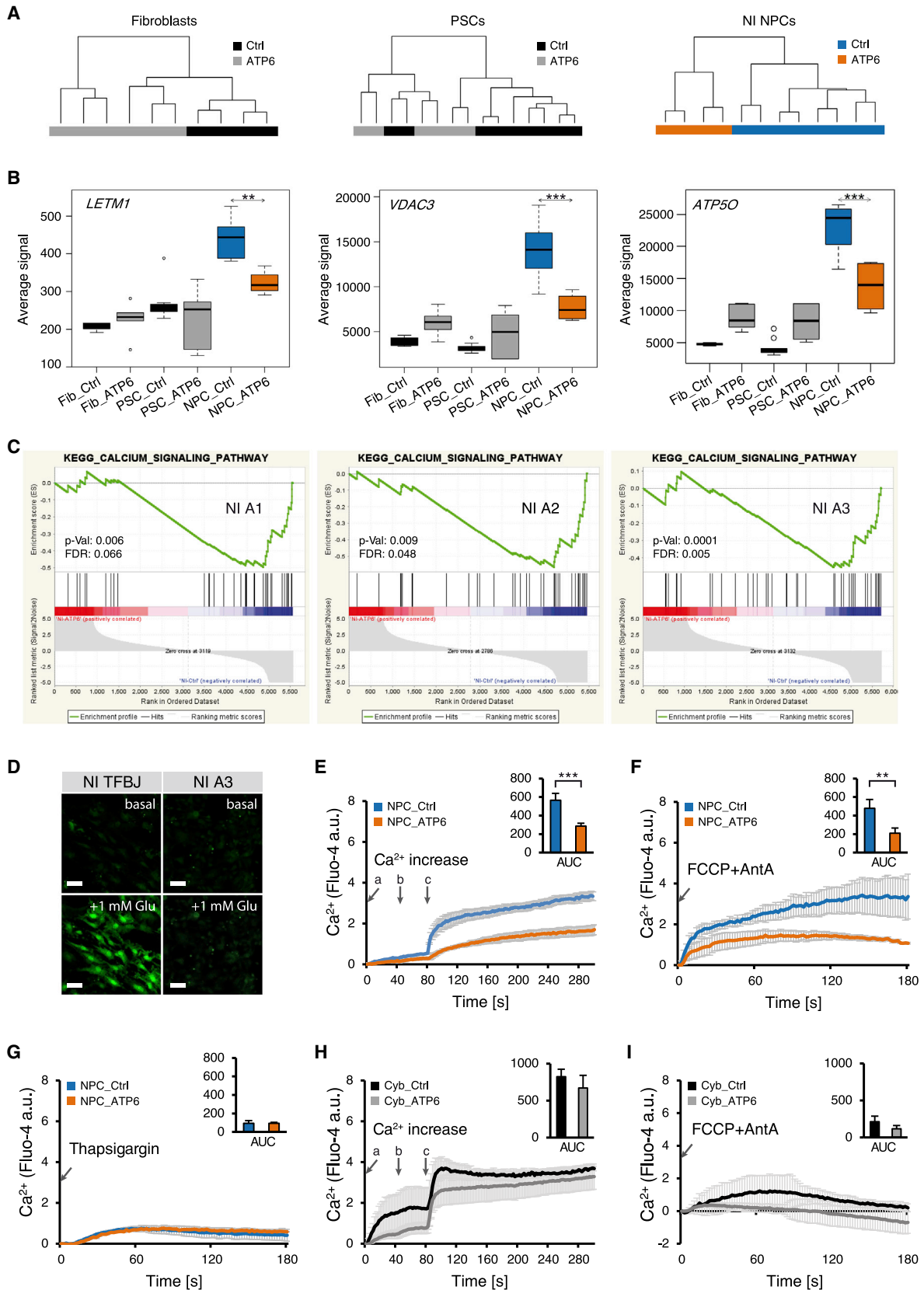
Phenotypic Compound Screenings in NPC_ATP6

We next sought to address whether NPCs might be suitable for drug discovery approaches, targeting the abnormal MMP phenotype identified in patient NPCs and confirmed in patient neurons. We adapted the imaging-based MMP assay to a 384-well-plate format that could be used with the HCS automated fluorescence microscope Cellomics ArrayScan (Figure 7A). As a proof of concept, we tested 130 compounds from a library of 700 FDA-approved drugs (Table S3) for effects on the cells' MMP. To overcome a degree of variability inherent in the assay, we used each compound in duplicate and repeated the same screening twice. To reduce the risk of false negatives, we focused on NI A2, the NPC_ATP6 line with the highest MMP. Each compound was used at a final concentration of 1 μM and was dissolved in 0.04% DMSO, a dose that we verified as non-toxic and with no direct influence on the MMP (Figures S7A and S7B). Ten compounds decreased the MMP of NI A2 down to -2 SD values (Figure 7B) without negatively affecting the cells' viability (Figures S7C and S7D).

We decided to focus on one of these compounds, avanafil (Figure 7B), a PDE5 inhibitor. The family of compounds to which this belongs is commonly used against erectile dysfunction in adults, and it is approved for pediatric use to treat pulmonary arterial hypertension (Archer and Michelakis, 2009). These compounds can cross the blood-brain barrier and have been reported to have positive effects on neurogenesis (García-Barroso et al., 2013; Rutten et al., 2008). We assessed avanafil's impact on bioenergetics and calcium homeostasis in patient-derived NPCs and differentiated neurons. Treatment with 1 μM avanafil overnight induced a slight but significant depolarization of mitochondria, similar in state 3 and state 4 respiration (Figures S7E and S7F). Despite this partial depolarization, there was no significant change in the rate of ATP production in NPC_ATP6 (Figure 7C). The ATP steady-state level remained constant also in patient neurons after exposure to the drug (Figure 7D).

Avanafil did not alter the profile of cytosolic calcium in NPC_ATP6 when increasing doses of external calcium were applied (Figures 7E and 7F). Importantly, however, the overnight treatment with avanafil increased the release of mitochondrial calcium when we triggered mitochondrial depolarization using FCCP and antimycin A in the three NPC_ATP6 lines, reaching significance in two of them (Figures 7G and 7H). Avanafil also induced a similar increase in mitochondrial calcium release in differentiated neurons carrying the *MT-ATP6* mutation (Figures 7I and 7J).

Overall, these data demonstrate that NI NPCs can be used successfully in phenotypic compound screenings with the aim of developing personalized drug discovery approaches for neurological mtDNA diseases (Figure S7G).

DISCUSSION

Technical and methodological limitations have impeded the development of models for the development of individualized approaches to diseases caused by mutations in mitochondrial genes. Here we describe an innovative system based on iPSC-derived NPCs that can be used both to discover the cellular mechanisms that these mutations disrupt and develop novel treatments based on screens or other methods.

We show that NPCs undergo functional mitochondrial maturation and develop oxidative metabolism in a way that resembles normal neuronal development. During this process, the cells preserve the patient-specific nuclear and mitochondrial matched genotypes. This is crucial in the study of mtDNA disorders, given that the nuclear background is thought to play a modulatory role in these diseases (Bénit et al., 2010; D'Aurelio et al., 2010), as illustrated by the phenotypic differences observed in patients with the same homoplasmic *MT-ATP6* mutation (Auré et al., 2013; Pitceathly et al., 2012). Hence, NPCs should be useful in dissecting the specific vulnerability of the nervous system to mtDNA diseases (Abramov et al., 2010; Carelli and Chan, 2014).

Figure 6. Altered Calcium Homeostasis in NPC_ATP6

(A) Hierarchical clustering is based on genes regulating mitochondrial calcium homeostasis (see Figure S6G) in Fib_Ctrl (BJ and HFF1), Fib_ATP6 (A1, A2, and A3), PSC_Ctrl (H1, H9, TDHFF1, TDBJ5, and TFBJ), PSC_ATP6 (TFA2, TDA2.3, and TDA3.1), NPC_Ctrl (NI H1, NI H9, NI TDBJ5, and NI TFBJ), and NPC_ATP6 (NI A2 and NI A3).

(B) Expression of three genes involved in mitochondrial calcium homeostasis. The p values were determined by ANOVA followed by a Tukey post hoc test between NPC_Ctrl and NPC_ATP6.

(C) Global proteomics were analyzed as pairwise comparison between NPC_ATP6 (NI A1, NI A2, and NI A3) and NPC_Ctrl (here shown in comparison to NI TFBJ, similar results were observed with NI H1, NI H9, and NI TFC1).

(D) Representative images of NPC_Ctrl (line NI TFBJ) and NPC_ATP6 (line NI A3) show basal cytosolic calcium before stimulation (basal) and at maximal peak Fluo-4 fluorescence after 1 mM glutamate (Glu) stimulation. Scale bar, 50 μm.

(E) Cytosolic calcium release by exposing permeabilized cells to increasing doses of calcium (a, 5 mM CaCl$_2$; b, 10 mM CaCl$_2$; and c, 50 mM CaCl$_2$ in Tyrode's solution). NPC_Ctrl (NI H1, NI TFBJ, NI TDBJ5, and NI TFC2; each with at least three biological replicates) was compared to NPC_ATP6 (NI A1, NI A2, and NI A3; each with at least four biological replicates).

(F) Calcium release from mitochondria in permeabilized cells following exposure to FCCP and antimycin A (both 1 μM). NPC_Ctrl (NI H1, NI TFBJ, NI TDBJ5, and NI TFC2; each with at least three biological replicates) was compared to NPC_ATP6 (NI A1, NI A2, and NI A3; each with at least four biological replicates).

(G) Calcium release from the endoplasmic reticulum (ER) in permeabilized cells treated with 1 μM thapsigargin. NPC_Ctrl (NI H1, NI H9, and NI TFBJ; each with at least two biological replicates) was compared to NPC_ATP6 (NI A2 and NI A3; each with at least three biological replicates).

(H) Cytosolic calcium increase in permeabilized cells following exposure to calcium (a: 5 mM CaCl$_2$, b: 10 mM CaCl$_2$, c: 50 mM CaCl$_2$ in Tyrode's solution) in Cyb_Ctrl (TFSR and 143B+) and Cyb_ATP6 (F06, F07, and F08) (at least three biological replicates each).

(I) Mitochondrial calcium release following exposure to FCCP and antimycin A (both 1 μM) in permeabilized Cyb_Ctrl (TFSR and 143B+) and Cyb_ATP6 (F06, F07, and F08) (at least three biological replicates each).

In (E)–(I), the inlays show the respective area under the curve (AUC) quantification. In all panels, unless otherwise indicated, error bars represent SEM and p values were determined by unpaired two-tailed Student's t tests (*p $\leq$ 0.05, **p $\leq$ 0.01, and ***p $\leq$ 0.001).

See also Figure S6, Table S1, and Movie S2.

(legend on next page)

CellPress
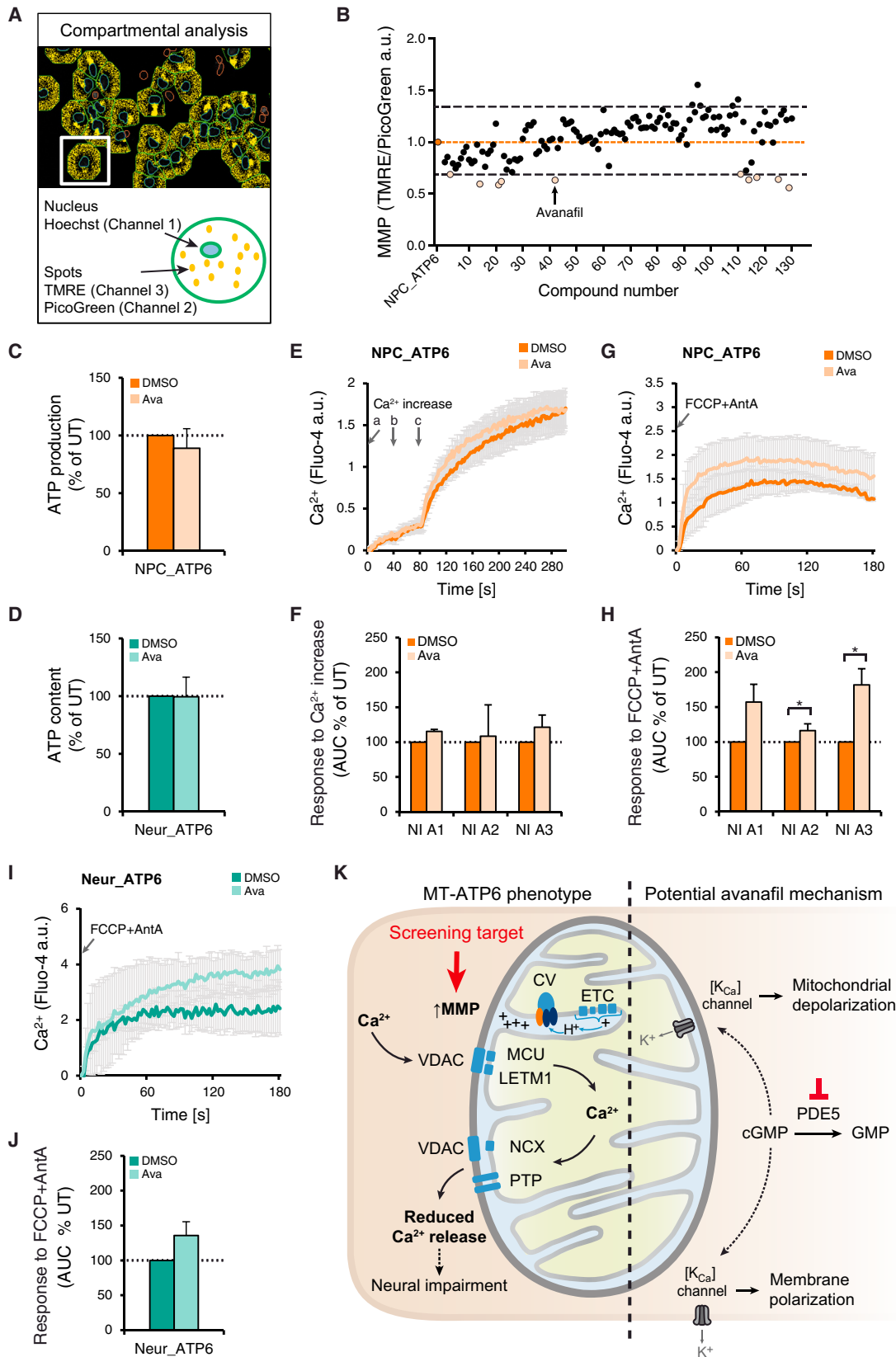
The approach described here for a homoplasmic mtDNA mutation should be equally applicable to heteroplasmic mutations. In fact, iPSC-derived NPCs retained the entire mtDNA profile of the initial fibroblasts, including even the hypervariable D-loop region. Studies have indicated that the induction to iPSCs may be associated with heteroplasmic mtDNA alterations (Folmes et al., 2013; Hämäläinen et al., 2013; Perales-Clemente et al., 2016; Prigione et al., 2011b). These variations appear to derive from the clonal origin of the iPSCs, because they also occur in clonally expanded fibroblasts (Kang et al., 2016; Ma et al., 2015). This means that the mtDNA sequence profile of patient-derived iPSC lines must be thoroughly assessed to ensure that the cells are suitable for use in drug discovery or other types of treatments.

Our finding that the *MT-ATP6* mutation disrupted mitochondrial calcium homeostasis specifically in NPCs, but not in fibroblasts or cybrids, may help explain the specificity of the defects it causes. Neuronal cells are particularly sensitive to changes in calcium handling (Neher and Sakaba, 2008), which is considered a major contributor to excitotoxic cell death (Orrenius et al., 2003). The occurrence of aberrantly reduced cytoplasmic calcium in NPC_ATP6 cells also might explain the beneficial effects observed when patients carrying the *MT-ATP6* mutation are treated with acetazolamide (Auré et al., 2013). Acetazolamide activates calcium-activated potassium $[K_{Ca}]$ plasma membrane channels, whose opening is hindered by reductions in the amount of cytosolic calcium (Sah and Faber, 2002). Our new data imply that targeting the MMP, which lies upstream of calcium dyshomeostasis, may be a useful strategy to address the neural impairment that develops through the mutation (Figure 7K). This fits with results from cellular and animal models, which showed that mild uncouplers can improve neural calcium homeostasis (Maragos and Korde, 2004).

Further work is needed to dissect the mechanisms responsible for the disruption of mitochondrial calcium homeostasis in NPC_ATP6 cells. Mitochondrial hyperpolarization, which promotes the sequestration of calcium into mitochondria (Rizzuto et al., 2012), might be responsible for the reduced mitochondrial calcium release observed in the cytoplasm. Another possibility is an impairment in the regulation of mitochondrial calcium efflux mechanisms, such as the sodium calcium exchanger (NCX) or the PTP, which forms from dimers of the ATP synthase (Giorgio et al., 2013) (Figure 7K).

We also carried out the first phenotypic small molecule screening in patient-derived NPCs, which led to our identification of the PDE5 inhibitor avanafil as a potential therapeutic agent for use in *MT-ATP6*-related encephalopathies. PDE5 inhibitors increase the intracellular level of cyclic GMP (cGMP), which in turn activates $[K_{Ca}]$ channels in both the plasma membrane and the inner mitochondrial membrane (Ahern et al., 2002; Szewczyk et al., 2006; Wang et al., 2008). The positive effects of avanafil on calcium homeostasis may thus be due to its effects on cellular polarization, which are similar to those of acetazolamide, and/or to its triggering of a slight mitochondrial depolarization, which would directly influence mitochondrial calcium homeostasis (Figure 7K). Yet another possibility is that PDE5 inhibitors affect the opening of the PTP (Ascah et al., 2011). Further studies will be needed to clarify the mode by which avanafil and PDE5 inhibitors act in the context of *MT-ATP6*-associated neural impairment. Future work will determine whether compounds identified in NPC_ATP6 might target mechanisms involved also in other mitochondrial disorders.

In conclusion, iPSC-derived NPCs appear well suited for use in drug-screening strategies aimed at developing treatments for neurological mitochondrial disorders. Live-cell-based HCS permits the simultaneous evaluation of mitochondrial parameters beyond MMP (Iannetti et al., 2016), and it might allow compound screenings aimed simultaneously at multiple mitochondrial phenotypes. The employment of FDA-approved libraries could speed up the process of translation to clinical applications

Figure 7. Phenotypic HCS in NPC_ATP6

(A) HCS-based quantification of MMP in live intact cells, using Hoechst for cell determination, TMRE for MMP, and PicoGreen for normalization over mtDNA content. Cellomics ArrayScan was employed according to the Compartmental Analysis BioApplication.

(B) Screening of 130 FDA-approved compounds (all 1 μM in 0.04% DMSO overnight). NPC_ATP6 (NI A2) treated overnight with 0.04% DMSO (dark orange) was used as baseline. Dashed lines refer to 2 SD distance from the baseline. Shown here are the average values (two biological replicates, each with two technical duplicates per compound).

(C) ATP production is shown in permeabilized NPC_ATP6 (NI A1, NI A2, and NI A3; two biological replicates each) exposed to either DMSO or 1 μM avanafil overnight (see Figure S7G).

(D) ATP content is shown in intact cells in Neur_ATP6 (from NI A2 and NI A3) after overnight treatment with DMSO or 1 μM avanafil (see Figure S7H).

(E) Cytoplasmic calcium increase following exposure to calcium (a, 5 mM CaCl₂; b, 10 mM CaCl₂; and c, 50 mM CaCl₂ in Tyrode's solution) in DMSO-treated NPC_ATP6 (DMSO) (lines NI A1, NI A2, and NI A3; each with at least four biological replicates) and in NPC_ATP6 treated with 1 μM avanafil overnight (Ava) (lines NI A1, NI A2, NI A3; each with at least three biological replicates).

(F) Area under the curve (AUC) quantification of the cytoplasmic calcium increase in NPC_ATP6 lines treated with either DMSO (DMSO) or avanafil (Ava).

(G) Mitochondrial calcium release upon exposure to FCCP and antimycin A (both 1 μM) in DMSO-treated NPC_ATP6 (DMSO) (lines NI A1, NI A2, and NI A3; each with at least four biological replicates) and in NPC_ATP6 treated with 1 μM avanafil overnight (Ava) (lines NI A1, NI A2, and NI A3; each with at least three biological replicates).

(H) Area under the curve (AUC) quantification of the mitochondrial calcium release in NPC_ATP6 lines treated with either DMSO (DMSO) or avanafil (Ava).

(I) Mitochondrial calcium release following exposure to FCCP and antimycin A (both 1 μM) in permeabilized DMSO-treated Neur_ATP6 (DMSO) (lines Neur_A2 and Neur_ A3) and in the same neurons treated overnight with 1 μM avanafil (Ava).

(J) Area under the curve (AUC) quantification of the mitochondrial calcium release in patient neurons (Neur_A2 and Neur_A3) treated with either DMSO (DMSO) or avanafil (Ava) (see Figure S7I).

(K) Left side: suggested mechanisms underlying the impaired mitochondrial calcium handling of NPC_ATP6 cells; right side: potential mode of action of avanafil (see Discussion for details). CV, complex V (*MT-ATP6* in orange); H, hydrogen ions (protons); ETC, electron transport chain (complexes I–IV); MCU, mitochondrial calcium uniporter; NCX, sodium-calcium exchanger; PTP, permeability transition pore; cGMP, cyclic GMP. In all panels, error bars represent SEM and p values were determined by unpaired two-tailed Student's t tests (*$p \leq 0.05$, **$p \leq 0.01$, and ***$p \leq 0.001$).

See also Figure S7 and Table S3.

CellPress

through drug repositioning (Ashburn and Thor, 2004). We believe that creating disease-relevant in vitro model systems, such as the one described here, may represent an essential step toward the identification of effective therapies for mtDNA diseases and other conditions that cannot yet be treated.

STAR★METHODS

Detailed methods are provided in the online version of this paper and include the following:

- KEY RESOURCES TABLE
- CONTACT FOR REAGENT AND RESOURCE SHARING
- EXPERIMENTAL MODEL AND SUBJECT DETAILS
  - Fibroblasts and cybrids
  - Pluripotent stem cells (PSCs)
  - rNPCs and eNPCs
- METHOD DETAILS
  - Derivation of iPSCs
  - Generation of NI NPCs
  - Neuronal and astrocyte differentiation
  - Calcium imaging
  - Whole mtDNA sequence analysis
  - Global transcriptomics
  - Global proteomics
  - PCR analysis
  - Immunostaining
  - Cell proliferation
  - Bioenergetic assessment
  - Transmission electron microscopy (TEM)
  - MMP quantification in permeabilized cells
  - Imaging-based MMP assessment in intact cells
  - High-content screening (HCS)
  - Mitochondrial reactive oxygen species (ROS) production
  - Electrophysiology
- QUANTIFICATION AND STATISTICAL ANALYSIS
- DATA AND SOFTWARE AVAILABILITY

SUPPLEMENTAL INFORMATION

Supplemental Information includes seven figures, five tables, and two movies and can be found with this article online at http://dx.doi.org/10.1016/j.stem.2016.12.013.

AUTHOR CONTRIBUTIONS

Conceptualization, A.P. and A.L.; Methodology, A.P., A.L., C.L., P.L., R.B., B.W., T.M., D.M., J.C.M., and M. Schuelke; Formal Analysis, M. Singh, B.M., and N.M.; Investigation, A.L., M. Schuelke, C.L., P.L., R.B., A.Z., G.I., K.A., M.L., O.Z., E.-M.L., V.P., B.F., J.E., M. Semtner, B.M., and D.M.; Resources, N.H.; Writing – Original Draft, A.P. and A.L.; Writing – Review & Editing, A.P. and A.L.; Supervision, A.P., A.L., M. Schuelke, Z.I., J.C.M., J.P., F.B., J.A., and E.E.W.; Visualization, C.L., A.P., and A.L; Funding Acquisition, A.P., A.L., and M. Schuelke.

ACKNOWLEDGMENTS

REFERENCES

Abramov, A.Y., Smulders-Srinivasan, T.K., Kirby, D.M., Acin-Perez, R., Enriquez, J.A., Lightowlers, R.N., Duchen, M.R., and Turnbull, D.M. (2010). Mechanism of neurodegeneration of neurons with mitochondrial DNA mutations. Brain 133, 797–807.

Ahern, G.P., Klyachko, V.A., and Jackson, M.B. (2002). cGMP and S-nitrosylation: two routes for modulation of neuronal excitability by NO. Trends Neurosci. 25, 510–517.

Archer, S.L., and Michelakis, E.D. (2009). Phosphodiesterase type 5 inhibitors for pulmonary arterial hypertension. N. Engl. J. Med. 361, 1864–1871.

Ascah, A., Khairallah, M., Daussin, F., Bourcier-Lucas, C., Godin, R., Allen, B.G., Petrof, B.J., Des Rosiers, C., and Burelle, Y. (2011). Stress-induced opening of the permeability transition pore in the dystrophin-deficient heart is attenuated by acute treatment with sildenafil. Am. J. Physiol. Heart Circ. Physiol. 300, H144–H153.

Ashburn, T.T., and Thor, K.B. (2004). Drug repositioning: identifying and developing new uses for existing drugs. Nat. Rev. Drug Discov. 3, 673–683.

Auré, K., Dubourg, O., Jardel, C., Clarysse, L., Sternberg, D., Fournier, E., Laforêt, P., Streichenberger, N., Petiot, P., Gervais-Bernard, H., et al. (2013). Episodic weakness due to mitochondrial DNA MT-ATP6/8 mutations. Neurology 81, 1810–1818.

Bénit, P., El-Khoury, R., Schiff, M., Sainsard-Chanet, A., and Rustin, P. (2010). Genetic background influences mitochondrial function: modeling mitochondrial disease for therapeutic development. Trends Mol. Med. 16, 210–217.

Brennand, K.J., Simone, A., Jou, J., Gelboin-Burkhart, C., Tran, N., Sangar, S., Li, Y., Mu, Y., Chen, G., Yu, D., et al. (2011). Modelling schizophrenia using human induced pluripotent stem cells. Nature 473, 221–225.

Campbell, M.D., and Marcinek, D.J. (2016). Evaluation of in vivo mitochondrial bioenergetics in skeletal muscle using NMR and optical methods. Biochim. Biophys. Acta 1862, 716–724.

Cardona, A., Saalfeld, S., Schindelin, J., Arganda-Carreras, I., Preibisch, S., Longair, M., Tomancak, P., Hartenstein, V., and Douglas, R.J. (2012). TrakEM2 software for neural circuit reconstruction. PLoS ONE 7, e38011.

Carelli, V., and Chan, D.C. (2014). Mitochondrial DNA: impacting central and peripheral nervous systems. Neuron 84, 1126–1142.

Childs, A.M., Hutchin, T., Pysden, K., Highet, L., Bamford, J., Livingston, J., and Crow, Y.J. (2007). Variable phenotype including Leigh syndrome with a 9185T>C mutation in the MTATP6 gene. Neuropediatrics 38, 313–316.

Cox, J., and Mann, M. (2008). MaxQuant enables high peptide identification rates, individualized p.p.b.-range mass accuracies and proteome-wide protein quantification. Nat. Biotechnol. 26, 1367–1372.

Cox, J., Hein, M.Y., Luber, C.A., Paron, I., Nagaraj, N., and Mann, M. (2014). Accurate proteome-wide label-free quantification by delayed normalization and maximal peptide ratio extraction, termed MaxLFQ. Mol. Cell. Proteomics *13*, 2513–2526.

D'Aurelio, M., Vives-Bauza, C., Davidson, M.M., and Manfredi, G. (2010). Mitochondrial DNA background modifies the bioenergetics of NARP/MILS ATP6 mutant cells. Hum. Mol. Genet. *19*, 374–386.

Deschauer, M., Krasnianski, A., Zierz, S., and Taylor, R.W. (2004). False-positive diagnosis of a single, large-scale mitochondrial DNA deletion by Southern blot analysis: the role of neutral polymorphisms. Genet. Test. *8*, 395–399.

Detjen, A.K., Tinschert, S., Kaufmann, D., Algermissen, B., Nurnberg, P., and Schuelke, M. (2007). Analysis of mitochondrial DNA in discordant monozygotic twins with neurofibromatosis type 1. Twin Res. Hum. Genet. *10*, 486–495.

Folmes, C.D., Nelson, T.J., Martinez-Fernandez, A., Arrell, D.K., Lindor, J.Z., Dzeja, P.P., Ikeda, Y., Perez-Terzic, C., and Terzic, A. (2011). Somatic oxidative bioenergetics transitions into pluripotency-dependent glycolysis to facilitate nuclear reprogramming. Cell Metab. *14*, 264–271.

Folmes, C.D., Martinez-Fernandez, A., Perales-Clemente, E., Li, X., McDonald, A., Oglesbee, D., Hrstka, S.C., Perez-Terzic, C., Terzic, A., and Nelson, T.J. (2013). Disease-causing mitochondrial heteroplasmy segregated within induced pluripotent stem cell clones derived from a patient with MELAS. Stem Cells *31*, 1298–1308.

Gandhi, S., Wood-Kaczmar, A., Yao, Z., Plun-Favreau, H., Deas, E., Klupsch, K., Downward, J., Latchman, D.S., Tabrizi, S.J., Wood, N.W., et al. (2009). PINK1-associated Parkinson's disease is caused by neuronal vulnerability to calcium-induced cell death. Mol. Cell *33*, 627–638.

García-Barroso, C., Ricobaraza, A., Pascual-Lucas, M., Unceta, N., Rico, A.J., Goicolea, M.A., Sallés, J., Lanciego, J.L., Oyarzabal, J., Franco, R., et al. (2013). Tadalafil crosses the blood-brain barrier and reverses cognitive dysfunction in a mouse model of AD. Neuropharmacology *64*, 114–123.

Giorgio, V., von Stockum, S., Antoniel, M., Fabbro, A., Fogolari, F., Forte, M., Glick, G.D., Petronilli, V., Zoratti, M., Szabó, I., et al. (2013). Dimers of mitochondrial ATP synthase form the permeability transition pore. Proc. Natl. Acad. Sci. USA *110*, 5887–5892.

Gorman, G.S., Schaefer, A.M., Ng, Y., Gomez, N., Blakely, E.L., Alston, C.L., Feeney, C., Horvath, R., Yu-Wai-Man, P., Chinnery, P.F., et al. (2015). Prevalence of nuclear and mitochondrial DNA mutations related to adult mitochondrial disease. Ann. Neurol. *77*, 753–759.

Hämäläinen, R.H., Manninen, T., Koivumäki, H., Kislin, M., Otonkoski, T., and Suomalainen, A. (2013). Tissue- and cell-type-specific manifestations of heteroplasmic mtDNA 3243A>G mutation in human induced pluripotent stem cell-derived disease model. Proc. Natl. Acad. Sci. USA *110*, E3622–E3630.

Hargus, G., Ehrlich, M., Araúzo-Bravo, M.J., Hemmer, K., Hallmann, A.L., Reinhardt, P., Kim, K.P., Adachi, K., Santourlidis, S., Ghanjati, F., et al. (2014). Origin-dependent neural cell identities in differentiated human iPSCs in vitro and after transplantation into the mouse brain. Cell Rep. *8*, 1697–1703.

Hazkani-Covo, E., Zeller, R.M., and Martin, W. (2010). Molecular poltergeists: mitochondrial DNA copies (numts) in sequenced nuclear genomes. PLoS Genet. *6*, e1000834.

Iannetti, E.F., Smeitink, J.A., Beyrath, J., Willems, P.H., and Koopman, W.J. (2016). Multiplexed high-content analysis of mitochondrial morphofunction using live-cell microscopy. Nat. Protoc. *11*, 1693–1710.

Inoue, K., Nakada, K., Ogura, A., Isobe, K., Goto, Y., Nonaka, I., and Hayashi, J.I. (2000). Generation of mice with mitochondrial dysfunction by introducing mouse mtDNA carrying a deletion into zygotes. Nat. Genet. *26*, 176–181.

Kang, E., Wang, X., Tippner-Hedges, R., Ma, H., Folmes, C.D., Gutierrez, N.M., Lee, Y., Van Dyken, C., Ahmed, R., Li, Y., et al. (2016). Age-related accumulation of somatic mitochondrial DNA mutations in adult-derived human iPSCs. Cell Stem Cell *18*, 625–636.

Kauppila, J.H., Baines, H.L., Bratic, A., Simard, M.L., Freyer, C., Mourier, A., Stamp, C., Filograna, R., Larsson, N.G., Greaves, L.C., and Stewart, J.B. (2016). A phenotype-driven approach to generate mouse models with pathogenic mtDNA mutations causing mitochondrial disease. Cell Rep. *16*, 2980–2990.

King, M.P., and Attardi, G. (1989). Human cells lacking mtDNA: repopulation with exogenous mitochondria by complementation. Science *246*, 500–503.

Kirches, E., Michael, M., Warich-Kirches, M., Schneider, T., Weis, S., Krause, G., Mawrin, C., and Dietzmann, K. (2001). Heterogeneous tissue distribution of a mitochondrial DNA polymorphism in heteroplasmic subjects without mitochondrial disorders. J. Med. Genet. *38*, 312–317.

Koch, P., Opitz, T., Steinbeck, J.A., Ladewig, J., and Brüstle, O. (2009). A rosette-type, self-renewing human ES cell-derived neural stem cell with potential for in vitro instruction and synaptic integration. Proc. Natl. Acad. Sci. USA *106*, 3225–3230.

Krencik, R., and Zhang, S.C. (2011). Directed differentiation of functional astroglial subtypes from human pluripotent stem cells. Nat. Protoc. *6*, 1710–1717.

Kulak, N.A., Pichler, G., Paron, I., Nagaraj, N., and Mann, M. (2014). Minimal, encapsulated proteomic-sample processing applied to copy-number estimation in eukaryotic cells. Nat. Methods *11*, 319–324.

Li, W., Sun, W., Zhang, Y., Wei, W., Ambasudhan, R., Xia, P., Talantova, M., Lin, T., Kim, J., Wang, X., et al. (2011). Rapid induction and long-term self-renewal of primitive neural precursors from human embryonic stem cells by small molecule inhibitors. Proc. Natl. Acad. Sci. USA *108*, 8299–8304.

Ma, H., Folmes, C.D., Wu, J., Morey, R., Mora-Castilla, S., Ocampo, A., Ma, L., Poulton, J., Wang, X., Ahmed, R., et al. (2015). Metabolic rescue in pluripotent cells from patients with mtDNA disease. Nature *524*, 234–238.

Maragos, W.F., and Korde, A.S. (2004). Mitochondrial uncoupling as a potential therapeutic target in acute central nervous system injury. J. Neurochem. *91*, 257–262.

Mitalipov, S., and Wolf, D.P. (2014). Clinical and ethical implications of mitochondrial gene transfer. Trends Endocrinol. Metab. *25*, 5–7.

Moslemi, A.R., Darin, N., Tulinius, M., Oldfors, A., and Holme, E. (2005). Two new mutations in the MTATP6 gene associated with Leigh syndrome. Neuropediatrics *36*, 314–318.

Neher, E., and Sakaba, T. (2008). Multiple roles of calcium ions in the regulation of neurotransmitter release. Neuron *59*, 861–872.

Orrenius, S., Zhivotovsky, B., and Nicotera, P. (2003). Regulation of cell death: the calcium-apoptosis link. Nat. Rev. Mol. Cell Biol. *4*, 552–565.

Perales-Clemente, E., Cook, A.N., Evans, J.M., Roellinger, S., Secreto, F., Emmanuele, V., Oglesbee, D., Mootha, V.K., Hirano, M., Schon, E.A., et al. (2016). Natural underlying mtDNA heteroplasmy as a potential source of intra-person hiPSC variability. EMBO J. *35*, 1979–1990.

Pfeffer, G., Horvath, R., Klopstock, T., Mootha, V.K., Suomalainen, A., Koene, S., Hirano, M., Zeviani, M., Bindoff, L.A., Yu-Wai-Man, P., et al. (2013). New treatments for mitochondrial disease-no time to drop our standards. Nat. Rev. Neurol. *9*, 474–481.

Pfiffer, V., and Prigione, A. (2015). Assessing the bioenergetic profile of human pluripotent stem cells. Methods Mol. Biol. *1264*, 279–288.

Pitceathly, R.D., Murphy, S.M., Cottenie, E., Chalasani, A., Sweeney, M.G., Woodward, C., Mudanohwo, E.E., Hargreaves, I., Heales, S., Land, J., et al. (2012). Genetic dysfunction of MT-ATP6 causes axonal Charcot-Marie-Tooth disease. Neurology *79*, 1145–1154.

Polster, B.M., Nicholls, D.G., Ge, S.X., and Roelofs, B.A. (2014). Use of potentiometric fluorophores in the measurement of mitochondrial reactive oxygen species. Methods Enzymol. *547*, 225–250.

Prigione, A., Fauler, B., Lurz, R., Lehrach, H., and Adjaye, J. (2010). The senescence-related mitochondrial/oxidative stress pathway is repressed in human induced pluripotent stem cells. Stem Cells *28*, 721–733.

Prigione, A., Hossini, A.M., Lichtner, B., Serin, A., Fauler, B., Megges, M., Lurz, R., Lehrach, H., Makrantonaki, E., Zouboulis, C.C., and Adjaye, J. (2011a). Mitochondrial-associated cell death mechanisms are reset to an embryonic-like state in aged donor-derived iPS cells harboring chromosomal aberrations. PLoS ONE *6*, e27352.

Prigione, A., Lichtner, B., Kuhl, H., Struys, E.A., Wamelink, M., Lehrach, H., Ralser, M., Timmermann, B., and Adjaye, J. (2011b). Human induced pluripotent stem cells harbor homoplasmic and heteroplasmic mitochondrial DNA mutations while maintaining human embryonic stem cell-like metabolic reprogramming. Stem Cells *29*, 1338–1348.

CellPress

Prigione, A., Rohwer, N., Hoffmann, S., Mlody, B., Drews, K., Bukowiecki, R., Blümlein, K., Wanker, E.E., Ralser, M., Cramer, T., and Adjaye, J. (2014). HIF1α modulates cell fate reprogramming through early glycolytic shift and upregulation of PDK1-3 and PKM2. Stem Cells 32, 364–376.

Reddy, P., Ocampo, A., Suzuki, K., Luo, J., Bacman, S.R., Williams, S.L., Sugawara, A., Okamura, D., Tsunekawa, Y., Wu, J., et al. (2015). Selective elimination of mitochondrial mutations in the germline by genome editing. Cell 161, 459–469.

Reinhardt, P., Glatza, M., Hemmer, K., Tsytsyura, Y., Thiel, C.S., Höing, S., Moritz, S., Parga, J.A., Wagner, L., Bruder, J.M., et al. (2013). Derivation and expansion using only small molecules of human neural progenitors for neuro-degenerative disease modeling. PLoS ONE 8, e59252.

Rizzuto, R., De Stefani, D., Raffaello, A., and Mammucari, C. (2012). Mitochondria as sensors and regulators of calcium signalling. Nat. Rev. Mol. Cell Biol. 13, 566–578.

Rutten, K., Basile, J.L., Prickaerts, J., Blokland, A., and Vivian, J.A. (2008). Selective PDE inhibitors rolipram and sildenafil improve object retrieval performance in adult cynomolgus macaques. Psychopharmacology (Berl.) 196, 643–648.

Sah, P., and Faber, E.S. (2002). Channels underlying neuronal calcium-activated potassium currents. Prog. Neurobiol. 66, 345–353.

Staples, J.F., and Buck, L.T. (2009). Matching cellular metabolic supply and demand in energy-stressed animals. Comp. Biochem. Physiol. A Mol. Integr. Physiol. 153, 95–105.

Stein, J.L., de la Torre-Ubieta, L., Tian, Y., Parikshak, N.N., Hernández, I.A., Marchetto, M.C., Baker, D.K., Lu, D., Hinman, C.R., Lowe, J.K., et al. (2014). A quantitative framework to evaluate modeling of cortical development by neural stem cells. Neuron 83, 69–86.

Subramanian, A., Tamayo, P., Mootha, V.K., Mukherjee, S., Ebert, B.L., Gillette, M.A., Paulovich, A., Pomeroy, S.L., Golub, T.R., Lander, E.S., and Mesirov, J.P. (2005). Gene set enrichment analysis: a knowledge-based approach for interpreting genome-wide expression profiles. Proc. Natl. Acad. Sci. USA 102, 15545–15550.

Szewczyk, A., Skalska, J., Głab, M., Kulawiak, B., Malińska, D., Koszela-Piotrowska, I., and Kunz, W.S. (2006). Mitochondrial potassium channels: from pharmacology to function. Biochim. Biophys. Acta 1757, 715–720.

Van Haute, L., Spits, C., Geens, M., Seneca, S., and Sermon, K. (2013). Human embryonic stem cells commonly display large mitochondrial DNA deletions. Nat. Biotechnol. 31, 20–23.

Vizcaíno, J.A., Côté, R.G., Csordas, A., Dianes, J.A., Fabregat, A., Foster, J.M., Griss, J., Alpi, E., Birim, M., Contell, J., et al. (2013). The PRoteomics IDEntifications (PRIDE) database and associated tools: status in 2013. Nucleic Acids Res. 41, D1063–D1069.

Wang, X., Fisher, P.W., Xi, L., and Kukreja, R.C. (2008). Essential role of mito-chondrial Ca2+-activated and ATP-sensitive K+ channels in sildenafil-induced late cardioprotection. J. Mol. Cell. Cardiol. 44, 105–113.

Yu, J., Chau, K.F., Vodyanik, M.A., Jiang, J., and Jiang, Y. (2011). Efficient feeder-free episomal reprogramming with small molecules. PLoS ONE 6, e17557.

CellPress

STAR★METHODS

KEY RESOURCES TABLE

REAGENT or RESOURCE	SOURCE	IDENTIFIER
Antibodies		
Mouse monoclonal anti-NESTIN, clone 10C2	Millipore	MAB5326
Rabbit polyclonal anti-PAX6	BioLegend	901301
Goat polyclonal anti-SOX2 (Y-17)	Santa Cruz	sc-17320
Mouse monoclonal anti-beta-tubulin (TUJ1), clone 2G10	Sigma-Aldrich	T8578
Mouse monoclonal anti-OCT-3/4 (C-10)	Santa Cruz	sc-5279
Rabbit polyclonal anti-LIN28	ProteinTech Europe	11724
TRA-1-81	Millipore	MAB4381
Mouse monoclonal anti-VIMENTIN, clone V9	Sigma-Aldrich	V6630
Guinea pig polyclonal anti-MAP2	Synaptic Systems	188 004
Rabbit polyclonal anti-GABA	Calbiochem	PC213L
Mouse polyclonal anti-GFAP	DakoCytomation	M076101
Mouse monoclonal anti-Ki-67, clone Ki-67	DakoCytomation	F 0788
Goat polyclonal anti-NANOG	R&D Systems	AF1997
Rabbit polyclonal anti-DACH1	ProteinTech Europe	10914-1-AP
Mouse monoclonal anti-SMA, clone 1A4	DakoCytomation	M0851
Goat polyclonal anti-SOX17	R&D Systems	AF1924
Rabbit polyclonal anti-HES5 (M-104)	Santa Cruz	sc-25395
Rabbit polyclonal anti-tyrosine hydroxylase	Millipore	AB152
SSEA-4	Developmental Studies Hybridoma Bank (DSHB)	MC-813-70
SSEA-3	DSHB	MC-631
SSEA-1	DSHB	MC-480
Biological Samples		
Patient fibroblasts A1, A2, and A3 carrying homoplasmic levels of the mutation m.9185T>C in the *MT-ATP6* gene	Dr. Anne Lombès	Auré et al., 2013
hNP1 Human Neural Progenitor Cells (from WA09)	Aruna Biomedicals	hNP7013.1
Brain-derived ex vivo adult human NPCs (eNPCs, Normal Human Neural Progenitor Cells, NHNP)	Lonza	PT-2599
Human ESC line H1	WiCell Research Institute	WA01
Human ESC line H9	WiCell Research Institute	WA09
Mutant cybrids carrying homoplasmic levels of the mutation m.9185T>C in the *MT-ATP6* gene	Dr. Anne Lombès	Auré et al., 2013
Control lines: see Table S5		
Chemicals, Peptides, and Recombinant Proteins		
Matrigel Matrix	BD Biosciences	356231
hLIF	Miltenyi Biotec	130-108-156
CHIR99021	Cayman Chemical	13122
SB431542	SelleckChem	S1067
Compound E	Calbiochem	15579
SAG	Enzo Life Sciences	ALX-270-426-M001
Poly-L-ornithine	Sigma-Aldrich	P4957
Laminin	Sigma-Aldrich	L2020
Thapsigargin	Sigma-Aldrich	T9033

(Continued on next page)

Continued

REAGENT or RESOURCE	SOURCE	IDENTIFIER
Fluo-4	Life Technologies	F14201
Pluronic F-127	Sigma-Aldrich	P2443
TMRE	Molecular Probes	T669
StemPro Accutase	Life Technologies	A1110501
Recombinant human CNTF	PeproTech	450-13
Rock inhibitor	Enzo Life Sciences	ALX-270-333-M005
FCCP	Sigma-Aldrich	C2920
Antimycin A	Sigma-Aldrich	A8674
Oligomycin	Sigma-Aldrich	75351
Rotenone	Sigma-Aldrich	R8875
N2	Life Technologies	17502048
B27	Life Technologies	17504044
bFGF	PeproTech	100-18B
BDNF	Miltenyi Biotec	130-096-286
db-cAMP	Sigma-Aldrich	D0260-100
Purmorphamine	Miltenyi Biotec	130-104-465
Vitamin C	Sigma-Aldrich	A4403
GDNF	Miltenyi Biotec	130-098-449
TGFbeta3	Miltenyi Biotec	130-094-007
FGF8	R&D Systems	4745-F8-050
BSA	Sigma-Aldrich	A9576
IGF	R&D Systems	291-G1-200
StemMACS iPS-Brew XF	Miltenyi Biotec	130-104-368
HEPES	Sigma-Aldrich	H4034
MycoZap Plus-CL	Lonza	VZA-2012
MitoSOX Red	Life Technologies	M36008
Rhodamine 123	Sigma-Aldrich	R8004
CCCP	Sigma-Aldrich	C2759
HumanHT-12 v4 Expression BeadChips	Illumina	BD-103-0204
Critical Commercial Assays		
Lactate Colorimetric/Fluorometric Assay Kit	BioVision	K607-100
Expand Long Template PCR System	Roche	11 681 834 001
RNA isolation RNeasy Mini Kit	QIAGEN	74106
FlexiGene DNA Kit	QIAGEN	51206
SYBR Green PCR Master Mix	Applied Biosystems,	4309155
LightCycler 480 SYBR Green I Master Mix	Roche	04707516001
CyQUANT Kit	Molecular Probes	C7026
ATPlite Luminescence Assay Kit	Perkin Elmer	6016941
Quant-iT PicoGreen dsDNA Assay Kit	Life Technologies	P7581
FlexiGene DNA kit	QIAGEN	51206
Seahorse XF Cell Mito Stress Test	Seahorse Bioscience, Agilent	103015-100
Deposited Data		
Microarray results	GEO database	accession number GEO: GSE70071
Mass spectrometry proteomics data	ProteomeXchange Consortium via PRIDE partner repository (Vizcaíno et al., 2013)	dataset identifier PRIDE: PXD004977

CellPress

Continued

REAGENT or RESOURCE	SOURCE	IDENTIFIER
Recombinant DNA		
Episomal plasmids (OCT4, SOX2, NANOG, KLF4)	Yu et al., 2011	Addgene pEP4 E02S EN2K
Episomal plasmids (OCT4, SOX2, SV40LT, KLF4)	Yu et al., 2011	Addgene pEP4 E02S ET2K
Episomal plasmids (c-MYC, LIN28)	Yu et al., 2011	Addgene pCEP4-M2L
Plasmid pGEM®-T Easy	Promega	A3600
Primers: see Table S4		
Software and Algorithms		
HCS BioApplications (Compartmental analysis, Neuronal profiling)	Cellomics ArrayScan Life Technologies	https://www.thermofisher.com/de/de/home/brands/thermo-scientific/cellomics.html
Geneious v6.0.5 software	Biomatters	https://www.geneious.com/
ViiA 7 Software	Applied Biosystems	https://www.thermofisher.com/de/de/home/technical-resources/software-downloads/applied-biosystems-viia-7-real-time-pcr-system.html
GeneMarker v1.51 software	SoftGenetics	http://www.softgenetics.com/GeneMarker.php
AxioVision V4.6.3.0 software	Zeiss	http://www.zeiss.de/mikroskopie/downloads/axiovision-downloads.html
TrakEM2 within the FIJI software package	Cardona et al., 2012	http://imagej.net/TrakEM2
GraphPad Prism Windows 5.04	GraphPad Software, Inc.	http://www.graphpad.com
Database for Annotation, Visualization and Integrated Discovery (DAVID)		https://david.ncifcrf.gov/
R/Bioconductor packages in the programming language R (version 3.1 or greater)		http://bioconductor.org/packages/release/bioc/html/lumi.html
Allen Brain Atlas		http://human.brain-map.org/static/download
MaxQuant (version 1.5.0.0)	Cox and Mann, 2008	http://www.coxdocs.org/doku.php?id=:maxquant:start
Gene set enrichment analysis (GSEA, v2.2.1)	Subramanian et al., 2005	http://software.broadinstitute.org/gsea/index.jsp
Other		
FDA-approved drugs (see Table S3)	Selleckchem	z65122

CONTACT FOR REAGENT AND RESOURCE SHARING

Further information and requests for reagents may be directed to, and will be fulfilled by, the Lead Contact, Alessandro Prigione (alessandro.prigione@mdc-berlin.de).

EXPERIMENTAL MODEL AND SUBJECT DETAILS

Fibroblasts and cybrids

All fibroblast and cybrid cultures were maintained in DMEM medium (GIBCO) containing 10% fetal bovine serum (FBS, GIBCO), MycoZap antibiotics (Lonza), non-essential amino acids, Pen/Strep, and sodium pyruvate (all GIBCO). The cultures were kept in a humidified atmosphere of 5% CO_2 at 37°C under atmospheric oxygen conditions.

The patient fibroblasts A1, A2, and A3, all harboring homoplasmic levels of the mutation m.9185T>C in the *MT-ATP6* gene, were previously characterized (Auré et al., 2013). Control fibroblasts included BJ, HFF1 (both from ATCC), Con1, Con2 (both kindly obtained from Dr. Sarah Doss, Charité University), and LR (from Prof. Markus Schülke, Charité University). Ethical approval was obtained by local authorities to use patient fibroblasts for iPSC derivation (IRB code #EA2/131/13) and approval from the State Office of Health and Social Affairs Berlin (LaGeSo) was obtained for the generation of human iPSCs using retroviruses (347/92-25).

Control cybrids and mutant cybrids carrying the m.9185T>C mutation were previously reported (Auré et al., 2013). The mutant cybrids represented three different clones derived from A1 fibroblasts.

Information regarding all individuals and control and patient lines utilized in this study are reported in Table S5.

Pluripotent stem cells (PSCs)

hESC lines (H1 and H9) were purchased from WiCell and used according to the German law (personal license to A.P., #AZ: 3.04.02/0077-E01).

Control iPSCs included lines previously generated via transduction (TD) of the four Yamanaka retroviral factors, here labeled as TDHFF1, TDBJ4, and TDBJ5, previously reported as iPS2 (Prigione et al., 2010) and iB4 and iB5 (Prigione et al., 2011a), respectively. The retrovirally derived OiPS6 control iPSC line was also previously reported (Prigione et al., 2011b).

All pluripotent stem cells (PSCs) were cultivated on mitotically-inactivated mouse embryonic fibroblasts (MEFs) grown on Matrigel (BD Bioscience)-coated plates, using KO-DMEM medium (GIBCO) containing 20% knock-out serum replacement (KSR, GIBCO), 8 ng/μl bFGF (PeproTech), MycoZap antibiotics, non-essential amino acids, Pen/Strep, and sodium pyruvate. For DNA and RNA isolation, PSCs were grown under feeder-free conditions on Matrigel-coated plates using DMEM/F12 medium supplemented with N2, B27, 0.05% BSA (all from GIBCO), 8 ng/μl bFGF, and non-essential amino acids, Pen/Strep, and sodium pyruvate. All PSCs were kept in a humidified atmosphere of 5% CO_2 at 37°C in 5% oxygen conditions.

rNPCs and eNPCs

Rosette-based NPCs (rNPCs) derived from the hESC line H9 were purchased from Aruna (hNP1, Aruna Biomedicals). Brain-derived ex vivo adult human NPCs (eNPCs) were bought from Lonza (Normal Human Neural Progenitor Cells, NHNP). All NPC cultures were kept in a humidified atmosphere of 5% CO_2 at 37°C under atmospheric oxygen conditions.

METHOD DETAILS

Derivation of iPSCs

Control or patient fibroblasts were transduced with four transgene-encoding (OCT4, SOX2, KLF4, and c-MYC) retroviruses to generate transduction (TD)-iPSCs. Alternatively, they were transfected with episomal plasmids (containing the same four factors plus NANOG, LIN28, and SVLT) using Amaxa Cell Line Nucleofector Kit R (Lonza) to generate transfection (TF)-iPSCs. Transfection of episomal plasmids (Yu et al., 2011) was conducted using Amaxa Cell Line Nucleofector Kit R (Lonza), as previously described (Prigione et al., 2014). Pluripotency of the generated lines was confirmed following previously published procedures (Prigione et al., 2010) using both in vitro embryoid bodies (EB)-based differentiation and teratoma formation (performed by EPO-GmbH). The karyotype was assessed by chromosomal analysis after GTG-banding performed at the Human Genetic Center of Berlin, Germany.

Generation of NI NPCs

We obtained neural induction (NI) NPCs following on a previous report (Li et al., 2011) with slight modifications. Briefly, 70% confluent PSCs were split and plated onto feeder-free Matrigel-coated dishes in DMEM/F12 medium. After 24 hr, conditions were switched to NI-E medium (Neurobasal:DMEM/F12 [1:1], N2 [1x], B27 [1x], hLIF [10 ng/ml], CHIR99021 [4 μM, Cayman Chemical], SB431542 [3 μM, SelleckChem], Compound E [0.1 μM, Calbiochem], BSA [0.05%], Pen/Strep, and L-glutamine). Medium was changed every other day. After one week, the cells were split as single cells using Accutase (Life Technologies) and further cultured in NI medium (Neurobasal:DMEM/F12 [1:1], N2 [1x], B27 [1x], hLIF [10 ng/ml], CHIR99021 [3 μM], SB431542 [2 μM], BSA [0.05%], Pen/Strep, MycoZap antibiotics, and L-glutamine). NI NPCs were then maintained in NI medium with change every other day. NI NPCs were split at ratios of 1:2 to 1:5 using a cell spatula when confluency reached 80%–100%.

Neuronal and astrocyte differentiation

For neuronal differentiation, NI NPCs were plated at different densities (1-3 x10^6 per well) onto surfaces coated with Matrigel, poly-L-ornithine [20 μg/ml], and laminin [5 μg/ml] (both Sigma-Aldrich). For GABAergic neuronal differentiation, NI NPCs were plated on Matrigel, poly-L-ornithine [30 μg/ml], and laminin [5 μg/ml] in GA medium (DMEM/F12, N2 [1x], L-glutamine, Pen/Strep) containing BDNF [20 ng/ml] and SAG [200 nM] (Enzo Life Sciences). After four to five weeks, neuronal-like cells were cultured in GA medium with BDNF [20 ng/ml], IGF [10 ng/ml], and db-cAMP [300 ng/ml]. The maturation phase was extended for several weeks to allow electrophysiological measurements. Generation of dopaminergic neurons was performed according to a previously published protocol (Reinhardt et al., 2013). NPCs grown on Matrigel were induced to differentiate for 8 days using a medium containing Neurobasal:DMEM/F12 [1:1], N2 [1x], B27 [1x], purmorphamine [1 μM], vitamin C [200 μM], and FGF8 [100 ng/ml] and for 2 additional days using a medium containing Neurobasal:DMEM/F12 [1:1], N2 [1x], B27 [1x], purmorphamine [500 nM], and vitamin C [200 μM]. Cells were then split using Accutase at 1:3 ratios and plated onto matrigel-coated dishes. Conditions were switched to the maturation medium containing Neurobasal:DMEM/F12 [1:1], N2 [1x], B27 [1x], vitamin C [200 μM], db-cAMP [500 μM], BDNF [10 ng/ml], GDNF [10 ng/ml], and TGFbeta3 [1 ng/ml]. Differentiating neurons were kept in these conditions and the medium was changed every other day.

To assess the efficiency of neuronal differentiation from control and patient NPCs, high-content screening (HCS)-based quantification of TUJ1-positive cells was performed. Briefly, NPCs were differentiated into dopaminergic neurons and plated on Matrigel-coated 96-well plates. Cells were grown for 4 weeks (see culture conditions above) and then fixed and stained with TUJ1 antibody and counter-stained with Hoechst (see below for details on staining method). TUJ1-postive cells were counted using the ''Neuronal profiling'' BioApplication protocol of the HCS microscopy Cellomics ArrayScan (XTI Infinity High Content Platform, Life Technologies).

The differentiation of NI NPCs into astrocytes was promoted by a standardized protocol (Krencik and Zhang, 2011) with slight modifications. In brief, NPCs were cultured as neurospheres in uncoated flasks with NI medium for 3 months during which progenitor clusters switched from neurogenic neurospheres to gliogenic astrospheres. To maintain their size during their expansion, spheres

were regularly triturated with a flame-polished Pasteur pipette with smoothened edges and a 0.2-0.5 mm aperture diameter. After 3 months, spheres were dissociated to single cells with enzymatic digestion using Accutase (Life Technologies), transferred to new flasks at a concentration of at least 100,000 cells/ml and allowed to form new clusters. This process was repeated for a further 30 days. For maturation, dissociated single cells were plated onto acid-etched, poly-L-ornithine - (40 μg/ml) and laminin-coated (40 μg/ml) coverslips at a density of 10,000 cells/cm^2 for 7 days. For this final stage, hLIF, CHIR99021 and SB431542 in NI medium were replaced by rhCNTF (10 ng/ml, PeproTech).

Calcium imaging

Calcium studies were carried out by plating cells on glass bottom microwell dishes (MatTek) and incubating them in Tyrode's solution (in mM: 129 NaCl, 5 KCl, 2 CaCl$_2$, 1 MgCl$_2$, 25 HEPES, 30 Glucose, pH 7.4) supplemented with 5 μM Fluo-4 (Life Technologies) and 0.02% Pluronic F-127 (Sigma) for 45 min at RT and 5% CO$_2$ in the dark. Fluorescence microscopy was performed using a Zeiss LSM780 confocal microscope system with a 20x objective, using time-series frames with an interval of 2 s. After baseline interval, stimuli diluted in Tyrode's solution were added, including high KCl (30 mM), L-glutamate (1 mM), FCCP and antimycin A (both 1 μM), or thapsigargin (1 μM). Alternatively, increasing doses of calcium (5 mM, 10 mM, 50 mM CaCl$_2$) were added in calcium-free Tyrode's solution (Gandhi et al., 2009). Preincubation with digitonin (0.2 mM) was included for the last three stimuli. For each biological replicate, 10-20 cells were measured. Traces in the graphs represent the normalized average fluorescence intensity change over time. For quantification, the area under the curve (AUC) of the whole Fluo-4 fluorescence peak area was determined using GraphPad Prism.

Whole mtDNA sequence analysis

Total genomic DNA was isolated from cultured cells with the FlexiGene DNA kit (QIAGEN). Two overlapping fragments, long 9,932 bp and 9,506 bp, were generated using the Expand Long Template PCR System (Roche). Fragments were separated by electrophoresis on 0.7% agarose gels. Both long fragments were also sequenced using the BigDye v1.3 protocol (Life Technologies) on an ABI3500 genetic analyzer (Applied Biosystems) using oligonucleotides placed at $\approx$400 bp intervals. Nested sequences were quality tested and aligned at the Cambridge reference sequence using the Geneious v6.0.5 software (Biomatters). Positions that deviated from the reference were annotated by the software and visually inspected.

Global transcriptomics

Total RNA was isolated using the QIAGEN isolation kit (QIAGEN) and quality-checked by Nanodrop analysis (Nanodrop Technologies, Wilmington, DE, USA). Biotin-labeled cRNA samples were produced and hybridized onto Illumina human-12 BeadChips (Illumina, San Diego, CA, United States). Samples included HFF1, BJ, A1, A2, A3, H1, H9, TDHFF1 (iPS2), TDBJ5 (iB5), TFBJ, TFA2, TDA2.3, TDA3.1, NI H1, NI H9, NI TDBJ5, NI TFBJ, NI A2, NI A3, eNPCs, rNPCs_Ar, and rNPCs_NI. Microarray analysis, PCA plot, and heatmaps were performed using the R/Bioconductor packages in the programming language R /version 3.1 or greater). Genes were considered significantly expressed with detection p values $\leq$ 0.01. Differential expression analysis was performed using the Illumina custom method, using differential p values $\leq$ 0.01, fold change ratio > 1.5. Pathway analysis was determined by mapping onto KEGG pathways using Database for Annotation, Visualization and Integrated Discovery (DAVID) (https://david.ncifcrf.gov/). We fetched the significance level of normalized expression values corresponding to probe ID using lumi R's (http://bioconductor.org/packages/release/bioc/html/lumi.html). Variance-stabilizing transformation (VST) was used to deal with sample replicates and robust spline normalization (RSN) for normalization. Significant samples (p value < 0.05) were further transformed onto log2 scale and their IDs were annotated according to the IlluminaHumanv3.db Bioconductor annotation data package. Expression values of multiple probes for one gene were assigned by their median, resulting in analyzing 34,586 genes for each sample. The list of genes regulating energy metabolism was based on the Human Glucose Metabolism PCR Array (SA Bioscience, http://www.sabiosciences.com), as previously described (Prigione et al., 2011a).

Microarray raw data for NPCs from different studies were obtained from the National Center for Biotechnology Information Gene Expression Omnibus database under the series accession GSE25673 (Brennand et al., 2011), GSE28595 (Li et al., 2011), GSE40556 (Reinhardt et al., 2013), GSE55107 (Hargus et al., 2014) and GSE57595 (Stein et al., 2014). Datasets were processed and normalized as above. In order to create a matrix of expression level for unique genes in each sample, the datasets were merged by their gene names representing median of their respective probes resulted in a total of 16,493 genes for 198 samples. Differential expression between samples from various datasets was performed by correction of batch effect arising from two different platforms and by normalizing each dataset to a sample of the same genotype in order to merge datasets for downstream analysis. The corrected batch effect was confirmed by Principal Component Analysis (PCA). Each gene value was further assigned as their relative abundance value, which corresponded to the expression value of the gene in each sample divided by its mean expression value across the samples. The resulting expression matrix was subjected to hierarchical clustering (Spearman correlation, average linkage) and p value threshold. Fold change of differential expression between samples on log2 scale was analyzed using linear and Bayesian model algorithms from limma (http://bioconductor.org/packages/release/bioc/html/lumi.html) and pairwise differential. Heatmaps displaying Z-score were generated with matrix hierarchically clustered. Similar comparative analysis was performed on datasets of different stages of brain development. Brain data was downloaded from Allen Brain Atlas data portal (http://human.brain-map.org/static/download) and a matrix of 17,282 genes and 508 samples was created for further analysis as mentioned above.

Global proteomics

NPC_Ctrl (lines NI H1, HI H9, NI TFBJ, NI TFC1) and NPC_ATP6 (lines NI A1, NI A2, NI A3) were harvested and lysed under denaturing conditions in a buffer containing 4% SDS, 0.1 M DTT, 0.1 M Tris pH 8.0. Lysates were sonicated and boiled at 95°C, each for 5 min. Proteins were precipitated in 100% acetone ON at −20°C and re-dissolved in a buffer containing 6 M GdmCL, 10 mM TCEP, 40 mM CAA, 100 mM Tris pH 8.5. A dilution buffer (10% acetone, 25 mM Tris pH 8.5) in the ratio 1:10 (lysate:buffer) was added. 1% of the total lysates were finally digested by 1 μg trypsin at 37°C, ON. Peptides were acidified with a final concentration of 1% formic acid. 10% of the digest was directly used for LC-MS/MS analysis, the remaining 90% were further fractionated by strong cation exchange (SCX) chromatography with the following 5 SCX buffers: 2, 3, 4, 5 and buffer X, according to (Kulak et al., 2014). Dried fractions were dissolved in 5% acetone, 2% formic acid and subsequently injected for LC-MS/MS analysis. LC-MS/MS was carried out by nanoflow reverse phase liquid chromatography (Dionex Ultimate 3000, Thermo Scientific, Waltham, MA) coupled online to a Q-Exactive Plus Orbitrap mass spectrometer (Thermo Scientific, Waltham, MA). Briefly, the LC separation was performed using a PicoFrit analytical column (75 μm ID × 40 cm long, 15 μm Tip ID (New Objectives, Woburn, MA)) in-house packed with 2.1-μm C18 resin (Reprosil-AQ Pur, Dr. Maisch, Ammerbuch-Entringen, Germany) under controlled temperature of 50°C. Peptides were eluted using a non-linear gradient from 2 to 40% solvent B over 180 min at a flow rate of 266 nl/min (solvent A: 99.9% H_2O, 0.1% formic acid; solvent B: 79.9% acetonitrile, 20% H_2O, 0.1% formic acid). 3kV were applied for nanoelectrospray generation. A cycle of one full FT scan mass spectrum (300−1750 m/z, resolution of 70 000 at m/z 200, AGC target 1e^6) was followed by 12 data-dependent MS/MS scans (200-2000 m/z, resolution of 35 000, AGC target 5e^5, isolation window 2 m/z) with normalized collision energy of 25 eV. Target ions already selected for MS/MS were dynamically excluded for 30 s. In addition, only peptide charge states between two to eight were allowed. The label-free software MaxLFQ (Cox et al., 2014), which is integrated into MaxQuant (version 1.5.0.0), was used for quantification (Cox and Mann, 2008) and searched against the human proteome database UniProtKB with 88.717 entries, released in 11/2014. A false discovery rate (FDR) of 0.01 for proteins and peptides and a minimum peptide length of 7 amino acids were required. A maximum of two missed cleavages was allowed for the tryptic digest. Cysteine carbamidomethylation was set as fixed modification, while N-terminal acetylation and methionine oxidation were set as variable modifications.

For comprehensive proteome data analysis, we applied gene set enrichment analysis (GSEA, v2.2.1) (Subramanian et al., 2005) in order to see if priori defined sets of proteins show statistically significant, concordant differences between patients and controls. The intensity of detected proteins of each data group was averaged and zero values were replaced by 2 prior to log2 transformation. We used GSEA standard settings, except the minimum size exclusion was set to 10 or 15 and C2 (collection of pathways) or C5 (1454 gene annotations) were used as gene set databases (http://software.broadinstitute.org/gsea/msigdb/index.jsp).

PCR analysis

For long-range mtDNA-PCR, products were generated with nested primers in order to prevent sequencing of the numerous nuclear pseudogenes of the mtDNA (Hazkani-Covo et al., 2010). Both long fragments were sequenced using the BigDye v1.3 protocol (Life Technologies) on an ABI3500 genetic analyzer (Applied Biosystems) using oligonucleotides placed at ≈400 bp intervals, as previously described (Detjen et al., 2007).

Gene expression analysis was performed by quantitative real-time PCR (qPCR) using SYBR Green PCR Master Mix and the ViiA 7 Real-Time PCR System (Applied Biosystems). For each target gene, cDNA samples and negative controls were measured in triplicates using 384-Well Optical Reaction Plates (Applied Biosystems). Relative transcript levels of each gene were calculated based on the 2−ΔΔCT method. Data were normalized to the housekeeping genes ACTB and GAPDH and are presented as mean log2 ratios in relation to control lines.

For mtDNA copy number, the analysis was carried out with qPCR using LightCycler 480 SYBR Green I Master Mix (Roche) with addition of 10 pM of each primer on a LC480 Roche instrument (Roche) as follows: 95°C for 10 min, 40 cycles (95°C for 15 s, 60°C or 62°C for 30 s, 72°C for 30 s), 1 cycle (95°C for 30 s, 60°C for 30 s, heating to 95°C and cooling to 37°C). mtDNA was quantified as copies per μl by amplification of a fragment of the 12S mtDNA gene, with a standard curve obtained from serial dilutions of the linearized plasmid pGEM®-T Easy (Promega) containing the 12S mtDNA gene. Nuclear DNA was quantified as ng per μl by amplification of the 4401 – 4601 region of the single-copy 28S nuclear gene, with a standard curve obtained from serial dilutions of DNA from control fibroblasts. The mtDNA copy number was then calculated as copies per ng nuclear DNA.

PCR-based restriction fragment length polymorphism (RFLP) analysis with the *MnlI* restriction enzyme of the m.9185T>C mutation was carried out according to a standardized protocol (Auré et al., 2013). Briefly, a 120 bp fragment of mtDNA was amplified from total DNA with Phusion polymerase (NEB) and *MT-ATP6* primers. The product was digested with *MnlI* (NEB; 1 hr at 37°C) and separated in 2.5% agarose gels. Wild-type (WT) mtDNA is cleaved by *MnlI* into two fragments of 90 and 30 bp. Similar DNA-based PCR approaches were employed to assess absence of episomal vectors using oriP primers and for fingerprinting of the generated iPSC lines using the primers D21S2055 and DS17S1290, as previously described (Prigione et al., 2010).

The analysis of D-loop polymorphisms was performed as described before (Kirches et al., 2001). Briefly, PCR was performed with a FAM labeled forward-primer and a non-labeled reverse-primer. The products were digested with HaeIII and the fluorescent fragment sizes were determined with the ABI3500 Genetic Analyzer using the GeneMarker v1.51 software (SoftGenetics). Signals were transformed into curve diagrams, and the integral below the curve was taken as the relative amount of the respective length fragment. mtDNA deletions was investigated using two different long-range PCR sets (Deschauer et al., 2004). All primer sequences are reported in Table S4.

Immunostaining

Cells were fixed with 4% paraformaldehyde (PFA, Science Services) for 20 min at RT and washed two times with PBS. For permeabilization, cells were incubated with blocking solution containing 10% FBS and 1% Triton X-100 (Sigma-Aldrich) in PBS with 0.05% Tween 20 (Sigma-Aldrich) (PBS-T) for 1 hr at RT. Primary antibodies included NESTIN (Millipore, 1:200), PAX6 (BioLegend, 1:200), SOX2 (Santa Cruz, 1:100), TUJ-1 (Sigma-Aldrich, 1:3000), OCT4 (Santa Cruz, 1:300), LIN28 (ProteinTech Europe, 1:300), VIMENTIN (Sigma-Aldrich, 1:300), MAP2 (Synaptic System, 1:100), GFAP (DakoCytomation, 1:20), GABA (Calbiochem, 1:10000), Ki-67 (Dako-Cytomation, 1:50), NANOG (R&D Systems, 1:200), DACH1 (ProteinTech Europe, 1:100), Smooth Muscle Actin (SMA) (DakoCytomation, 1:200), SOX17 (R&D Systems, 1:50), HES5 (Santa Cruz, 1:50), TH (Millipore, 1:300), and TRA1-81 and SSEA1/3/4 (from Hybridoma Bank, all 1:200). Primary antibodies were diluted in blocking solution and incubated for at least 1 hr at RT. Prior to and following the 1 hr incubation period with the corresponding secondary antibody (Alexa Fluor, 1:300, Life Technologies), cells were washed once in PBS-T and two times in blocking solution, 5 min each. Counterstaining of nuclei was achieved by incubation with 100 ng/ml 4',6-diamidino-2-phenylindole (DAPI, Vector Laboratories) in PBS for 1 hr at RT. All images were acquired using the confocal microscope LSM510 Meta (Zeiss) in combination with the AxioVision V4.6.3.0 software (Zeiss) and further processed with Adobe Photoshop CS-6 (Adobe Systems).

Cell proliferation

PSCs (H1, TFBJ, 8 replicates each) were seeded as single cells at a density of 10,000 cells/well in black-wall, clear-bottom plates (Corning) (coated with Matrigel) in normal StemMACS iPS-Brew XF medium (Miltenyi Biotec GmbH, 130-104-368). 10 μM Rock inhibitor (Enzo, ALX-270-333-M005) was added 2 hr before splitting and also after seeding, to promote single-cell survival. Cells were allowed to attach and recover for 72 hr, before changing medium to normal E8 medium (containing 25 mM glucose) or E8-galactose medium (glucose-free, with 10 mM galactose). After the medium change one plate was fixed (day 0). Additional plates were fixed on the following three days at the same time every day.

Other cells (patient and control fibroblasts, NI NPCs, and cybrids) were seeded at a density of 5,000, 20,000 and 40,000 cells/well in black-wall, clear-bottom plates (Corning) (coated with Matrigel for NPCs) in normal DMEM (containing 25 mM glucose) or DMEM-galactose (glucose-free, with 10 mM galactose) for fibroblasts and cybrids and NI medium (containing 25 mM glucose) or NI-galactose (glucose-free, with 10 mM galactose) for NI NPCs. Cells were allowed to attach for one hour, before one plate was fixed (day 0). Additional plates were fixed on the following three days at the same time every day.

For fixation, cells were washed with PBS, incubated for 20 min in 4% PFA and 8.1 μM Hoechst, and washed again with PBS for final storage. The analysis was performed both using fluorescence reading with a Tecan plate reader (Infinite M200) and the count of Hoechst (33342, Invitrogen) -positive spots according to the "spot detector" function of the high-content screening (HCS) analyzer Cellomics ArrayScan (see below). All data were normalized to values obtained at day 0 to obtain a relative proliferation curve.

Bioenergetic assessment

Live assessment of cellular bioenergetics was performed using Seahorse XF24 extracellular flux analyzer (Seahorse Bioscience), as described previously (Pfiffer and Prigione, 2015). Briefly, 40,000 cells were plated into each Matrigel-coated well of the XF24 well plates and incubated overnight at 37°C with 5% CO_2. Assays were initiated by removing the growth medium and replacing it with unbuffered media. The cells were incubated at 37°C for 60 min to allow media temperature and pH to reach equilibrium before starting the simultaneous measurement of mitochondrial respiration (oxygen consumption rate, OCR) and anaerobic glycolysis (extracellular acidification rate, ECAR). After baseline records, four additions (all products at 1 μM and from Sigma) were performed to test mitochondrial respiration functions. First oligomycin, a complex V blocker, inhibited OXPHOS and tested respiration coupling to ATP synthesis. Two consecutive administrations of FCCP, a protonophore uncoupling agent, decreased the MMP, therefore increasing respiration rate, and enabled the quantification of the maximal respiration under maximal mitochondrial uncoupling. The last injection of rotenone, a complex I blocker, and antimycin A, a complex III blocker, caused complete inhibition of mitochondrial respiration, thereby allowing us to probe the non-respiratory oxygen consumption. Normalization to DNA content in each well of the plate was performed using the CyQUANT Kit (Molecular Probes).

Cellular ATP content was determined with the luciferase-based ATPlite Luminescence Assay Kit (Perkin Elmer), according to the provider's instructions (Prigione et al., 2010). Briefly, 7000 cells were seeded in 100 μl medium per well in a 96-well plate and subsequently lysed with 50 μl of a solution that at the same time inactivates the endogenous ATPases. Further addition of 50 μl substrate solution containing Luciferase and Luciferin allows quantification of luminescence occurring upon the reaction with ATP. The emitted light is proportional to the ATP concentration in the cells and was measured with a Tecan plate reader (Infinite M200). Every sample was measured at least in triplicate. Results are presented as picomoles of ATP per 1000 cells.

Extracellular lactate amount was quantified using a Lactate Colorimetric/Fluorometric Assay Kit (BioVision). Briefly, cells were seeded in a 96-well plate at a density of 40,000 cells/well and incubated overnight. The next day, medium was replaced by unbuffered media and incubated for 3 hr. Subsequently, the supernatants were collected and lactate measurement was performed according to the manufacturer's instructions. Samples were prepared in triplicates and mixed 1:1 with a reaction mix containing enzymes and a lactate probe to proportionally produce fluorescence that could be measured with a Tecan plate reader (Infinite M200). Normalization by DNA content was accomplished using CyQUANT (Molecular Probes). Results were presented as picomoles of lactate per well per DNA content.

ATP production was carried out as previously described (Auré et al., 2013). Briefly, cells diluted in 1 mM EGTA, 3 mM EDTA, 5 mM K phosphate and 100 mM K MES pH 7.2 were permeabilized with 20 μg digitonin per million cells. Protein concentration was measured before addition of 0.8% fatty acid free bovine serum albumin. 100 000 cells were incubated with 10 mM pyruvate, 10 mM glutamate, 5 mM malate, 20 mM succinate, 50 μM Ap5A (an adenylate kinase inhibitor), and 1 mM ADP. ATP steady state was then measured at 4 min interval (T_0 T_4), followed by addition of 8 μM antimycin A and 1 μM oligomycin and again ATP steady state measurement at 4 min interval (T'_0 T'_4). The production of ATP was calculated as $[(T_4 - T_0) - (T'_4 - T'_0)]/(4 \times \text{prot concentration})$ and expressed as nanomoles ATP produced per minute and mg proteins.

Transmission electron microscopy (TEM)

All cells were grown on coated Thermanox plastic coverslips (Nalge Nunc International) and fixed with 2.5% glutaraldehyde in 50 mM sodium cacodylate buffer (pH 7,4) supplemented with 50 mM sodium chloride for at least 30 min at RT. Specimens were washed in the same buffer and post-fixed for 1.5 hr in 0.5% osmium tetroxide at RT, followed by 0.1% tannic acid for 30 min and 2% uranyl acetate for 1,5 hr. Samples were dehydrated in a graded series of ethanol, embedded in Spurr's resin (Low Viscosity Spurr Kit, Ted Pella, Inc) and polymerized at 60°C. Ultra-thin sections (70 nm) were prepared using an ultra-microtome (Reichert Ultracut E, Leica) and mounted on copper TEM grids from. Sections were counter stained with uranyl acetate and lead citrate. Micrographs were recorded at varying nominal magnifications using a Philips CM100 microscope operated at 100 kV, which was equipped with a 1k F114 Fastscan CCD camera (TVIPS) or a Tecnai Spirit microscope operated at 120 kV, which was equipped with a 2k Eagle CCD camera (FEI). For ultrastructural analysis, areas covering entire neuronal cells were imaged automatically on the Tecnai Spirit microscope using the MSI-Raster application within the Leginon system. Regions of interest (up to 50×50 μm^2) were selected at low magnification (560x) and successively imaged at 4400x and 15000x magnification applying a defocus of -100 μm and -4 μm, respectively. Obtained micrographs were then montaged to single images using TrakEM2 within the FIJI software package (Cardona et al., 2012).

MMP quantification in permeabilized cells

Cells were diluted in 1 mM EGTA, 3 mM EDTA, 5 mM K phosphate and 100 mM K MES pH 7.2 and permeabilized with 20 μg digitonin per million cells. Addition of 0.8% fatty acid free bovine serum albumin and 200 nM rhodamine 123 was followed by distribution of the cells in four bioenergetic conditions: resting basal state = 10 mM glutamate and 5 mM malate, state 3 respiration = 10 mM glutamate, 5 mM malate and 1 mM ADP, state 4 respiration = 10 mM glutamate, 5 mM malate, 1 mM ADP and 1 μM oligomycin, and complete depolarization = 10 mM glutamate, 5 mM malate, 1 mM ADP, 1 μM oligomycin, 8 μM antimycin A and 10 μM CCCP (carbonyl cyanide m-chlorophenyl hydrazone, a protonophore dissipating the inner membrane potential). Fluorescence signal was read on an Accuri C6 flow cytometer after gating the cell population based on forward and size scatters. Mitochondrial membrane potential was then calculated using the Nernst equation and 1% as the volume occupied by mitochondria in the volume of medium illuminated by the laser beam.

Imaging-based MMP assessment in intact cells

Cellomics ArrayScan (XTI Infinity High Content Platform, Life Technologies) was used for automated fluorescence microscopy analysis of MMP. One day prior to the assay, cells were collected by Accutase isolation and seeded on a black-wall, clear-bottom plate coated with Matrigel at a density of 40,000 or 80,000 cells/well on 96-well plates (Falcon) and incubated in NI medium overnight at 37°C, 5% CO_2. On the day of the assay, live cells were stained for 30 min with 10 nM TMRE (Molecular Probes, Life Technologies) for MMP and 3 μl/ml PicoGreen (Quant-iT PicoGreen dsDNA Assay Kit, Life Technologies) for mtDNA content normalization. Control staining was performed in parallel in cells exposed to 1 μM FCCP and 1 μM antimycin A (both from Sigma) to cause complete mitochondrial depolarization. All cells were then washed with PBS and stained with 1:10,000 Hoechst (33342, Invitrogen) diluted in phenol red-free-DMEM for 10 min at RT (or 37°C). After additional PBS washes, cells were kept in phenol red-free-DMEM for the duration of the assay. Images and analysis of Hoechst, TMRE and PicoGreen stainings were conducted with the Cellomics ArrayScan microscope according to the "Compartmental Analysis" BioApplication. The MMP values were extrapolated from the Cellomics measurements using the formula: TMRE (spot intensity * spot count) / PicoGreen (spot intensity * spot count). The results were calculated for each sample by subtracting the MMP value of the sample treated with FCCP and antimycin A from the MMP value of the sample under untreated conditions. The data are then presented in the paper as (TMRE / PicoGreen, a.u.).

High-content screening (HCS)

For the proof-of-principle compound screening, 130 compounds were taken from a library of 700 FDA-approved drugs (Selleckchem- z65122) (Table S3). The potentiometric TMRE probe signal was normalized to the signal of the fluorescent DNA dye Pico-Green. NI medium (see supplemental text for details) was supplemented with HEPES (Thermo Fisher) to allow the stable quantification of live MMP in a position-independent manner within 384-well plates. Briefly, 15,000 cells/well were plated on 384-well plates (Falcon) the day before the screening and a final concentration of 1 μM of the compounds was added. The second day, the medium was removed and the cells were stained with 10 nM TMRE and 3 μl/ml of PicoGreen together with 1:50,000 Hoechst diluted in phenol red-free NI medium for 30 min at 37°C, 5% CO_2. Control staining was performed in parallel with cells exposed to 1 μM FCCP and 1 μM antimycin A (both from Sigma) to induce complete mitochondrial depolarization. After one washing step with NI medium without supplements, cells were kept in phenol red-free NI medium for the duration of the assay.

Each compound was used at a concentration of 1 μM dissolved in 0.04% DMSO and tested in duplicate. The same screening was repeated twice and the values shown in Figure 7C represent the average of all the replicates. In every HCS plate, the control line NI H1 was included to control for inter-plate variability. Compound-treated and DMSO-treated cells were left overnight in NI medium and assessed for live MMP using 10 nM TMRE and 3 μl/ml of PicoGreen together with 0.2 μg/ml Hoechst (Invitrogen) diluted in phenol red-free NI medium. Treatment with FCCP and antimycin A (both 1 μM, Sigma) was used as positive control. HCS was conducted with Cellomics ArrayScan microscope (Thermo Fisher) and analyzed according to the "Compartmental Analysis" BioApplication.

Mitochondrial reactive oxygen species (ROS) production

The rate of mitochondrial ROS production was measured using the mitochondria-specific probe MitoSOX Red (Life Technologies). After incubation in normal or glucose-free medium for 4 hr, cells were harvested in their culture medium, 5×10^5 cells were loaded with 5 μM MitoSOX Red at 37°C during 10 min and analyzed by flow cytometry at different time points during 20 min. After gating on cells, the median fluorescence intensity was calculated for each time point and plotted as a function of time. The relative increase in fluorescence intensity per minute was used to eliminate the bias introduced by different dye accumulation due to MMP variation (Polster et al., 2014).

Electrophysiology

NPCs and neuronal cells were probed on coated coverslips. An EPC-7 amplifier and Patchmaster software (HEKA) were used for patch clamp recordings. Patch pipettes, made from borosilicate glass (Science Products, Hofheim, Germany), had resistances of 3-7 MΩ when filled with the intracellular solution containing (in mM): potassium gluconate (110), KCl (25), NaCl (5), $CaCl_2$ (0.5), $MgCl_2$ (1), EGTA (5) and HEPES (30). The standard extracellular solution (E1) (pH 7.4) contained (in mM): NaCl (140), KCl (5), $MgCl_2$ (1), $CaCl_2$ (2), HEPES-NaOH (10) and glucose (10). Series and input resistances were checked throughout the whole duration of each experiment by applying −5 mV-pulses in the voltage clamp mode at −50 mV.

Resting membrane potential was determined in the current clamp mode at 0 pA. Action potential generation of NPCs and neurons was measured in the current clamp mode by applying a holding current of −5 to −30 pA, so that the membrane potential was −70 mV. Increasing current pulses (300 ms; 5 pA to 50 pA) were applied every 5 s to evoke action potentials, if any. All patch clamp experiments were performed at room temperature (20–25°C).

QUANTIFICATION AND STATISTICAL ANALYSIS

Data were expressed as mean and standard deviation (mean ± SD) or standard error of the mean (mean ± SEM) where normality of the distribution could be verified, or as median and quartiles (median [1st;4th quartiles]) otherwise. For all experiments, multiple technical replicates and biological replicates were utilized. Detailed information regarding the number of replicates for each experiment can be found in the respective figure legend.

Significance was assessed using parametric tests (Student's t test, ANOVA) for normally-distributed data and non-parametric tests (Mann-Whitney U test, Kruskal-Wallis) when normal distribution could not be verified. Data were analyzed using GraphPad-Prism software (Prism 4.0, GraphPad Software, Inc.), Veusz (http://home.gna.org/veusz/), and Microsoft Excel (Microsoft).

DATA AND SOFTWARE AVAILABILITY

The accession number for the microarray transcriptomics data reported in this paper is GEO: GSE70071. The accession number for the mass spectrometry proteomics data reported in this paper is PRIDE: PXD004977 (http://proteomecentral.proteomexchange.org) (Vizcaíno et al., 2013).